International Journal of Mechanical Sciences 327 (2026) 111864

Contents lists available at ScienceDirect

International Journal of Mechanical Sciences

journal homepage: www.elsevier.com/locate/ijmecsci

Ori-DID: a direct inverse design method for origami structures

Tianshu Wang [a], Zhitao Su [a], Wenli Liu [a], Jiayao Ma [a,b,*], Yan Chen [a,b,*]

[a] School of Mechanical Engineering, Tianjin University, 135 Yaguan Road, Tianjin, 300350, China
[b] Key Laboratory of Mechanism Theory and Equipment Design of Ministry of Education, Tianjin University, 135 Yaguan Road, Tianjin, 300350, China

ARTICLE INFO

Keywords:
Inverse design
Origami structures
Deployable structures
Contact modelling
Dynamic relaxation
Multi-configuration morphing

ABSTRACT

Origami structures have been widely used in engineering applications as deployable structures and metamaterials Conventional designs tend to involve either experience-based forward design or iteration-based inverse design, making the synthesis of structures under more complex design objectives and constraints difficult to achieve This paper proposes a direct inverse design method for origami structures By adopting the dynamic relaxation method and maintaining isometry constraints for origami structures via bar length coupling, optimiser-free form-finding is achieved, enabling the synthesis of origami patterns without iterative computation Complex surface fitting objectives are imposed as external surface-normal forces during dynamic relaxation, while a contact force modelling scheme covering all possible panel collision scenarios is developed to enforce panel interference constraints By representing objectives and constraints as forces and solving the dynamic relaxation problem using an implicit Euler scheme, highly nonlinear behaviours can be captured with minimum computational cost, achieving the simultaneous dimensional and configurational synthesis of origami structures Using this method, example structures with multiple target configurations are synthesised This work provides a new tool for the direct inverse design of origami structures.

1. Introduction

Origami structures have seen extensive use in a wide range of fields, including aerospace [1–4], architecture [5,6], healthcare [7,8], robotics [9–11], and more, making their analysis and design an important topic The diverse spectrum of origami structures, including rigid-foldable [12–14], non-rigid [15–17], and curved-crease patterns [18–20], has been treated as mechanisms, deformable structures, or a combination of both, leading to a range of analysis and design methods With the continued development of computational tools, problems that were impossible for pen-and-paper work have now become approachable, leading to new discoveries and designs However, inverse design still requires a thorough analysis of individual design problems and heavy iterative computation using numerical optimisation, leaving an efficient and widely-applicable direct inverse design method still elusive.

Current computational design of origami structures involves rule-based approaches and, more often, optimization approaches Rule-based approaches [21–23] essentially abstract known rules in origami design to algorithmically generate desired patterns in a systematic and automated way The Origamizer software [24] makes extensive use of rules to generate complex shapes, while more engineering-oriented examples include thickness accommodation in flasher origami patterns [1,4,25] On the other hand, optimizers based on gradient descent or Newton solvers allow free-form shapes to be designed under developability and flat-foldability constraints [26–28], while extensive work has been completed for the surface fitting of Miura-ori patterns [29–32] Meanwhile, global optimization approaches including Bayesian optimization [33,34], genetic algorithms [35–37], and particle swarm optimization [38,39] have also been used for various designs As illustrated in Fig. 1a, however, optimization-based approaches necessitate an external optimization process, whose iterative nature greatly hinders computation efficiency.

One new approach for the direct inverse design of origami structures is dynamic relaxation With roots stemming from the 1960s [40–42], the dynamic relaxation method essentially reformulates an optimization problem, specifically a form-finding problem, into a structural dynamics problem Fictitious mass and damping are introduced to create a pseudo-dynamic system Explicit time integration is then formulated, with kinetic damping dissipating energy at velocity peaks, enabling the structure to trace a fictitious trajectory towards a minimum-energy equilibrium under prescribed loads and boundary conditions, thereby generating the desired structural form This method is useful for the

* Corresponding authors.
E-mail addresses: jiayao.ma@tju.edu.cn (J. Ma), yan_chen@tju.edu.cn (Y. Chen).

https://doi.org/10.1016/j.ijmecsci.2026.111864
Received 7 April 2026; Received in revised form 10 June 2026; Accepted 25 June 2026
Available online 28 June 2026
0020-7403/© 2026 Elsevier Ltd. All rights are reserved, including those for text and data mining, AI training, and similar technologies.

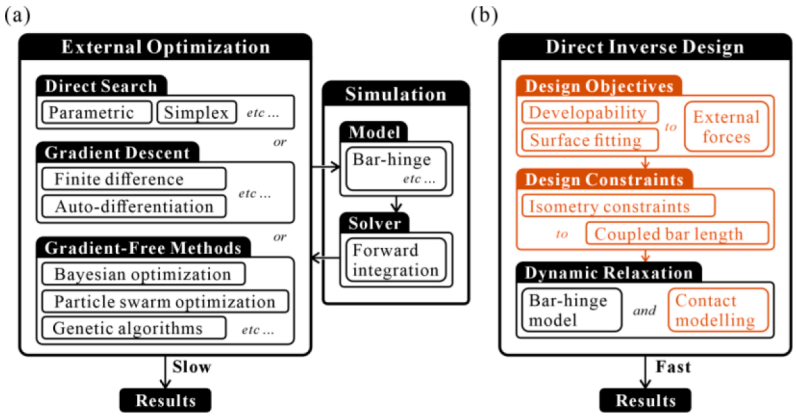

Fig. 1. Comparison between conventional inverse design methods and direct inverse design using dynamic relaxation (a) Conventional methods involve forward simulation and an external optimization loop, resulting in high computation cost (b) The direct inverse design method produces results in a single forward computation, where dynamic relaxation accommodates translated design objectives and constraints.

design of shell and membrane structures [43,44], tensegrity structures [45], combined tensegrity and membrane structures [46], and mesh reflectors [47], and offers high computational efficiency [48] While the aforementioned cases only consider a single state, origami design needs to consider multiple coupled states, at the very least an unfolded state and a folded state Specifically, the isometry of panels must be respected between states, while fold angles must be allowed to differ To this end, work on the strain energy minimization of origami shell reflectors [49] has demonstrated that multiple states can be simultaneously considered by imposing equality constraints [50] For more efficient design of general origami structures, this paper translates complex design objectives and constraints into equivalent forces and applies a coupled bar length scheme This circumvents computationally expensive equality constraints and harnesses the ability of a dynamics model to capture a highly non-linear form-finding process, not only adjusting the shape of individual panels, but also the overall folding configuration of the entire origami pattern, simultaneously realising both dimensional synthesis and configuration synthesis As Fig. 1b shows, this is a single forward process that is far more computationally efficient.

When developing a design method for origami structures, a significant challenge is analysing and accommodating both rigid-foldable and non-rigid origami patterns Most current methods are specialised for a single type of origami Rigid-foldable origami patterns can be analysed using mechanism theory approaches, including the Denavit-Hartenberg (DH) notation [51–53] and screw systems [54,55] More dedicated schemes focusing on crease rotation have been developed around rotation matrices [56] and quaternions [57], while other methods include directly describing rigid body motion constrained by vertex coincidence [33,34] or using singular value decomposition to extract instantaneous degree-of-freedom (DOF) and movement direction [58] On the other hand, non-rigid patterns [59,60] including curved-crease patterns [18,61] require panel deformation in addition to crease rotation, and thus cannot be analysed as mechanisms Applicable analysis methods include dedicated models based on geometric considerations [62], and more commonly, finite element methods [63,64], which consider origami as shell structures with specified panel and crease stiffness behaviours.

Over the past decade, bar-hinge models have become a dominant method for the unified analysis of rigid-foldable and non-rigid origami structures [65,66] By triangulating panels and considering creases as both axial and torsional springs, both rigid-foldable and non-rigid origami can be described With sufficient rod stiffness, rigid-foldable patterns can be simulated accurately, while sufficient division of panels allows deformation in non-rigid and curved-crease patterns to be resolved Popular implementations include the MERLIN model [67,68], which solves a quasi-static problem with an arc-length scheme, and the Origami Simulator [69], which solves a dynamics problem using the explicit Euler method The bar-hinge model has been implemented for non-trivial problems including multi-DOF rigid-foldable origami [70], curved-crease patterns [71], multi-layer origami structures [72] and more general shell structures [73] Adopting bar-hinge models for direct inverse design provides the necessary foundation for dynamic relaxation form-finding of both rigid-foldable and non-rigid origami structures.

One important omission in current bar-hinge models, however, is contact modelling Most implementations simply allow panels to pass through one another In the MERLIN code, folding angle is limited by a non-linear constitutive model applied to torsion springs [67] This however does not address the contact between non-adjacent panels For collision detection, point cloud methods have been applied to finite-thickness panels [33,34] Such an approach is versatile for complex shapes, but does not provide contact force information In thin-panel simulation, contact can be simplified to triangle-triangle collision [74] This has been applied [75] and includes contact forces, but multiple triangle-triangle collision scenarios exist, and certain scenarios remain unresolved Developing a model to cover the full range of collision scenarios is necessary for the direct inverse design method to ensure generated patterns are interference-free.

This paper presents a direct inverse design method applicable to both rigid-foldable and non-rigid origami patterns As Fig. 1 illustrates, the method incorporates dynamic relaxation based on a bar-hinge model with contact modelling which covers all possible collision scenarios Design objectives and constraints are translated into equivalent forces, while isometry constraints are modelled by a coupled bar length scheme, so that solutions can be obtained directly, free of external optimization processes and equality constraints The entire model is implemented in MATLAB as a self-contained package, and typical designs can be completed within minutes on a personal computer Section 2 introduces the bar-hinge model used here, including how contact is modelled within the bar-hinge framework to cover all possible scenarios Section 3 proposes the use of dynamic relaxation with a coupled bar length scheme, where design objectives are translated into external forces Dimensional and configuration synthesis of origami structures are demonstrated using several example designs, including multi-configuration morphing origami structures Finally, Section 4 presents concluding remarks.

2. Bar-hinge model with complete contact simulation

This section introduces the bar-hinge model implementation, which provides the foundation for subsequent direct inverse design Graph representation of origami structures is first introduced to provide a design framework Subsequently, the bar-hinge formulation and the accompanying dynamics simulation scheme are introduced Finally, a

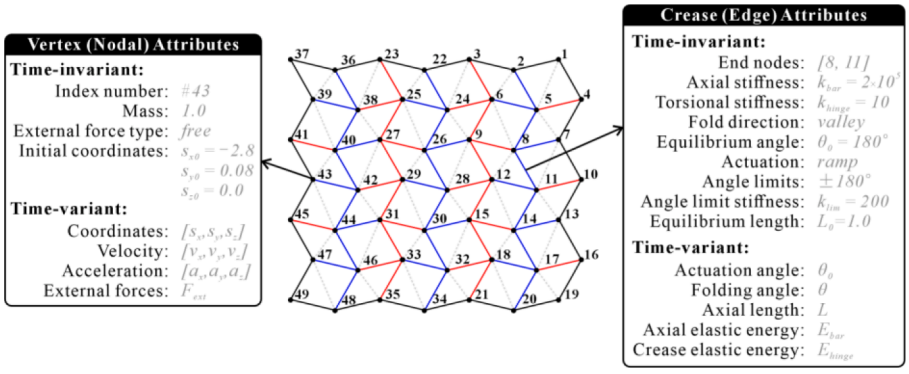

Fig. 2. Graph representation of an example double-corrugated origami pattern Time-invariant and time-variant attributes are assigned to vertices and edges.

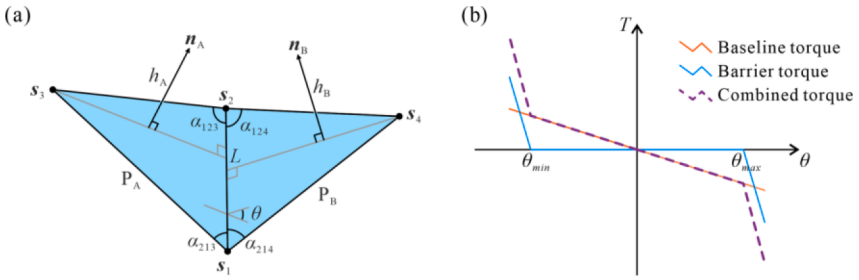

Fig. 3. Formulation of the basic bar-hinge element (a) The basic N4B5 bar-hinge element used in this implementation (b) Piece-wise linear torsional constitutive model used for implementing folding angle limits.

new contact modelling scheme is proposed to provide efficient identification and contact modelling of all possible triangle-triangle collision scenarios necessary for the generation of interference-free structures.

2.1. Graph representation of origami patterns

A well-organised description of origami patterns is essential for building a smooth pipeline covering simulation, direct inverse design, and post-processing Therefore, a graph representation is used to encapsulate the key parameters in an origami pattern Fig. 2 illustrates the description of a double-corrugated origami pattern as an instance The pattern includes 49 nodes and 120 edges, corresponding to the vertices and creases of the origami pattern A number of attributes are assigned to each node and edge The MATLAB implementation in this paper assumes a consistent system of units is used, and uses degrees for angular values.

Each node in the origami pattern include time-invariant and time-variant attributes Index number n_i identifies the node, and mass m refers to concentrated nodal mass External force type assigns the node into groups that are subject to different forces Here, for example, the node is free Nodes can also be subject to more complex forces representing design objectives and constraints, which are discussed in more detail in Section 3 Initial nodal coordinates $[s_{x0}, s_{y0}, s_{z0}]$ encode the geometry of the origami pattern and are described in a global Cartesian frame, which is maintained throughout the implementation On the other hand, time-variant variables are described as a time-series, and include the instantaneous coordinates $[s_x, s_y, s_z]$, velocity $[v_x, v_y, v_z]$, acceleration $[a_x, a_y, a_z]$ and total external forces $[F_{ext,x}, F_{ext,y}, F_{ext,z}]$ on the node at each time-step.

Each edge in the origami pattern also contain both time-invariant and time-variant attributes End nodes $[n_i, n_j]$ describe the index number of the nodes on either side of the edge, providing unique identification for the edge Axial and torsional stiffness k_{bar} and k_{hinge} are the linear stiffness assigned to the bar and hinge components of the bar-hinge model Fold direction describes the mountain-valley assignment of the crease, and the corresponding equilibrium angle θ_0 is the angle towards which hinge stiffness applies torque, which can be ramped with respect to time Angle limits $[\theta_{min}, \theta_{max}]$ constrain the folding angle A large restoring torque is applied when the folding angle exceeds these limits, dictated by angle limit stiffness k_{lim} Equilibrium length L_0 describes the zero-strain length of the crease, which constant during forward simulation, and updated during inverse design Regarding time-variant attributes, actuation angle $\theta_0(t)$ is the instantaneous equilibrium angle, which in this case is ramped Folding angle $\theta(t)$ describes the hinge's instantaneous position Axial length L denotes the instantaneous length of the bar element when strained Corresponding instantaneous axial and torsional elastic energies E_{bar} and E_{hinge} are also logged.

2.2. Bar-hinge element formulation

In the bar-hinge formulation here, the conventional N4B5 type bar-hinge element [66] is used Panels with >3 sides are represented by multiple triangular panels, whose shared creases are assigned a large stiffness to maintain shape As Fig. 3a shows, the basic element contains 4 vertices with coordinates $\boldsymbol{s}_i$, and 5 connecting bars, forming two adjacent panels P_A and P_B hinged at a shared crease.

The forces exerted on the four vertices in the bar-hinge element are a superposition of bar reaction forces and hinge reaction torques For the bar component, considering vertices with vector coordinates $\boldsymbol{s}_1$ and $\boldsymbol{s}_2$, the forces exerted on each vertex by bar elements would be

$$\boldsymbol{F}_{bar,s1} = k_{bar}(L - L_0)(\boldsymbol{s}_2 - \boldsymbol{s}_1) \tag{1}$$

and

$$\boldsymbol{F}_{bar,s2} = k_{bar}(L - L_0)(\boldsymbol{s}_1 - \boldsymbol{s}_2) \tag{2}$$

respectively, where k_{bar} is the axial stiffness of the bar between $\boldsymbol{s}_1$ and $\boldsymbol{s}_2$, L_0 is the strain-free length of the bar, and L is the instantaneous length at each time step Meanwhile for the hinge component, considering the two panels P_A and P_B with relevant vertex coordinates $\boldsymbol{s}_1$, $\boldsymbol{s}_2$, $\boldsymbol{s}_3$ and $\boldsymbol{s}_4$, the forces exerted by hinge torque on each vertex are

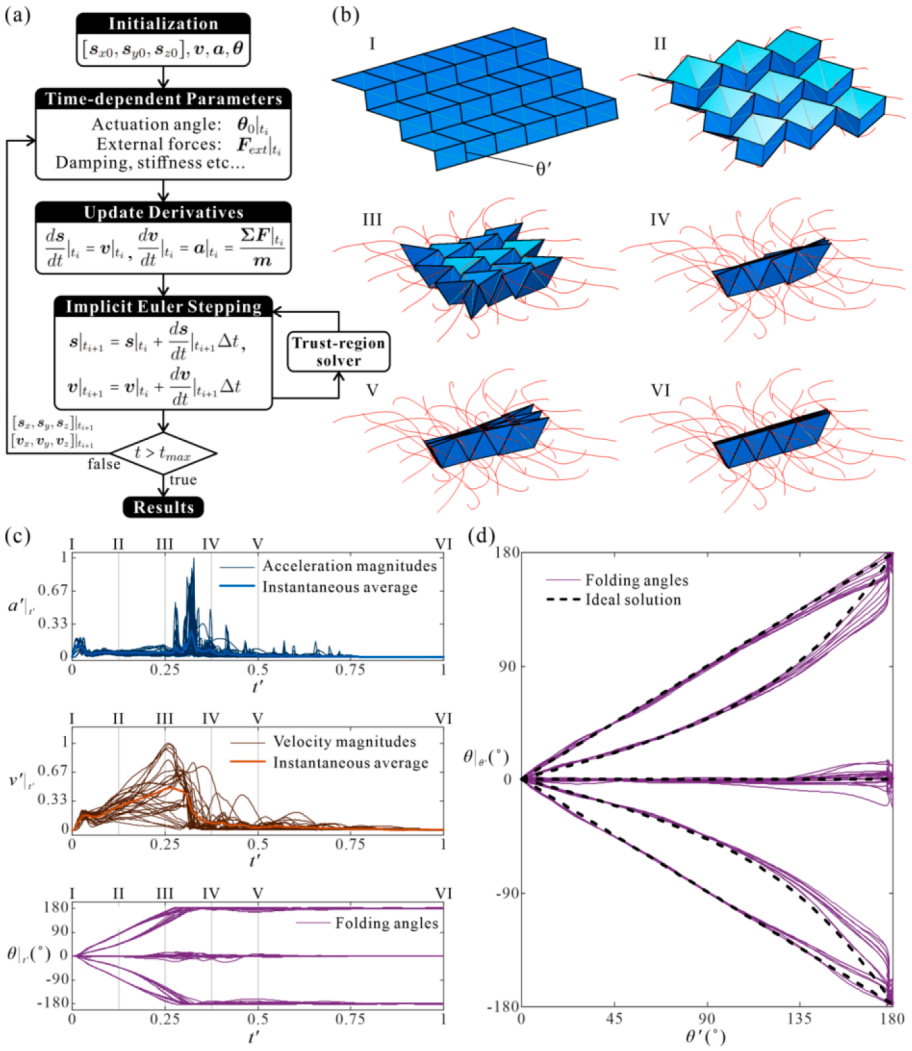

Fig. 4. Dynamics modelling using the bar-hinge model (a) Computation scheme based on the implicit Euler method (b) Folding simulation of an example Miura-ori structure (c) Normalised nodal accelerations, normalised nodal velocities, and folding angles, showing dynamic behaviour (d) Comparison of folding angle against the ideal kinematic solution of the Miura-ori pattern.

$$\boldsymbol{F}_{hinge,s1} = k_{hinge}(\theta-\theta_0)\left(\frac{\cot\alpha_{123}}{\cot\alpha_{213}+\cot\alpha_{123}}\frac{\boldsymbol{n}_A}{h_A}+\frac{\cot\alpha_{124}}{\cot\alpha_{214}+\cot\alpha_{124}}\frac{\boldsymbol{n}_B}{h_B}\right), \tag{3}$$

$$\boldsymbol{F}_{hinge,s2} = k_{hinge}(\theta-\theta_0)\left(\frac{\cot\alpha_{213}}{\cot\alpha_{213}+\cot\alpha_{123}}\frac{\boldsymbol{n}_A}{h_A}+\frac{\cot\alpha_{214}}{\cot\alpha_{214}+\cot\alpha_{124}}\frac{\boldsymbol{n}_B}{h_B}\right), \tag{4}$$

$$\boldsymbol{F}_{hinge,s3} = k_{hinge}(\theta-\theta_0)\left(\frac{\boldsymbol{n}_A}{h_A}\right) \tag{5}$$

and

$$\boldsymbol{F}_{hinge,s4} = k_{hinge}(\theta-\theta_0)\left(\frac{\boldsymbol{n}_B}{h_B}\right), \tag{6}$$

where $\boldsymbol{n}_A$ and $\boldsymbol{n}_B$ are the unit normal vectors of panels P_A and P_B, h_A and h_B are panel heights as measured from their shared edge, angles α_{ijk} denote in-plane angles between vertices $\boldsymbol{s}_i$, $\boldsymbol{s}_j$ and $\boldsymbol{s}_k$, θ and θ_0 are the instantaneous and equilibrium folding angles between the two panels, while restoring torque is represented by the term $k_{hinge}(\theta-\theta_0)$ Regarding energies, the linear model used here allows bar and hinge energy components to be calculated conveniently as

$$E_{bar} = \frac{1}{2}k_{bar}(L-L_0)^2 \tag{7}$$

and

$$E_{hinge} = \frac{1}{2}k_{hinge}(\theta-\theta_0)^2 \tag{8}$$

Fig. 3b shows how angle limits are enforced The baseline torque refers to the linear torque response provided by the basic bar-hinge element A barrier torque is superposed on this baseline torque in order to constrain the folding angle to desired limits θ_{min} and θ_{max}, formulated as

$$T|_{\theta>\theta_{max}} = k_{lim}(\theta-\theta_{max}) \tag{9}$$

and

$$T|_{\theta<\theta_{min}} = k_{lim}(\theta-\theta_{min}) \tag{10}$$

respectively, which can be added into Eqs. (3)-(6) and Eq. (8) An example case showing how the barrier torque enforces folding angle limits can be found in Appendix B.

Damping is critical for the steady-state stability of the dynamics model, and for convergence of the dynamic relaxation method For

simplicity, direct viscous nodal damping is used, meaning damping force is proportional to nodal velocity in the global frame of reference, given as

$$\boldsymbol{F}_{damping} = -C\frac{\mathrm{d}\boldsymbol{s}}{\mathrm{d}t}, \tag{11}$$

where $\frac{\mathrm{d}\boldsymbol{s}}{\mathrm{d}t}$ refers to nodal velocity and C is a specified damping coefficient.

2.3. Dynamics simulation

With the basic bar-hinge model formulated, origami simulation can be completed using different schemes A dynamics model is adopted here to provide the prerequisite for direct inverse design using dynamic relaxation It treats both rigid-foldable and non-rigid origami structures as deformable bar-hinge structures With sufficient bar and hinge stiffnesses, rigid-foldable structures can be modelled to sufficient fidelity.

Initialization uses the origami pattern's initial coordinates [$\boldsymbol{s}_{x0}$,$\boldsymbol{s}_{y0}$, $\boldsymbol{s}_{z0}$], while velocity is assigned as zero by default The vector notation here denotes values for all nodes in the origami pattern Initial angles and accelerations are calculated from coordinates and velocities using the bar-hinge constitutive model Time-dependent parameters include the aforementioned actuation angles and external forces, as well as nodal damping, bar and hinge stiffnesses, and other values of choice The full state-space description of the dynamic system is completed by a combination of nodal coordinates and nodal velocities at each time step The time-derivatives of the full system are hence

$$\frac{\mathrm{d}\boldsymbol{s}}{\mathrm{d}t}|_{t_i} = \boldsymbol{v}|_{t_i} \tag{12}$$

and

$$\frac{\mathrm{d}\boldsymbol{v}}{\mathrm{d}t}|_{t_i} = \boldsymbol{a}|_{t_i} = \frac{\Sigma\boldsymbol{F}|_{t_i}}{\boldsymbol{m}}, \tag{13}$$

where acceleration can be formulated as $\frac{\Sigma\boldsymbol{F}|_{t_i}}{\boldsymbol{m}}$, i.e., the sum of external forces and internal (bar-hinge) forces exerted on each node divided by nodal mass.

An implicit Euler scheme is used here for its simplicity and unconditional numerical stability, which tests have proven is crucial for capturing non-linear effects, including collisions and snap-through behaviour The corresponding backwards integration is formulated as

$$\boldsymbol{s}|_{t_{i+1}} = \boldsymbol{s}|_{t_i} + \frac{\mathrm{d}\boldsymbol{s}}{\mathrm{d}t}|_{t_{i+1}}\Delta t \tag{14}$$

and

$$\boldsymbol{v}|_{t_{i+1}} = \boldsymbol{v}|_{t_i} + \frac{\mathrm{d}\boldsymbol{v}}{\mathrm{d}t}|_{t_{i+1}}\Delta t, \tag{15}$$

where Δt is a prescribed time-step, $\boldsymbol{s}|_{t_i}$ and $\boldsymbol{v}|_{t_i}$ are known, $\boldsymbol{s}|_{t_{i+1}}$ and $\boldsymbol{v}|_{t_{i+1}}$ are unknown, while $\frac{\mathrm{d}\boldsymbol{s}}{\mathrm{d}t}|_{t_{i+1}}$ and $\frac{\mathrm{d}\boldsymbol{v}}{\mathrm{d}t}|_{t_{i+1}}$ are dependent MATLAB's *fsolve* function, a trust-region solver, is used to solve for $\boldsymbol{s}|_{t_{i+1}}$ and $\boldsymbol{v}|_{t_{i+1}}$ that satisfy Eqs. (14) and 15 Regarding computational efficiency of the solution process, large time-steps can be used by the implicit Euler method without hindering solution accuracy or stability, and to further accelerate the solution process, the Jacobian matrix of the coupled system is analytically derived and provided to *fsolve* This involves assembling the stiffness matrix of the bar-hinge model and deriving the derivatives of external forces and damping The overall workflow of the dynamics model is illustrated in Fig. 4a.

A Miura-ori origami structure is simulated to demonstrate key characteristics of the dynamics model developed here Fig. 4b shows the folding sequence, while Fig. 4c plots key values from the simulation Here, the transverse mountain and valley creases of the Miura-ori pattern are actuated, ramping towards ± 180° Inspecting relevant values presented in Fig. 4c, it can be seen that accelerations are initially low, then display several spikes between states III and IV when folding angle limits of ± 180° are reached, and creases bounce against the angle limit before settling at the fully folded state Correspondingly, velocities are initially high and drop when the folding angle limits are hit The inertial and damping effects included in the dynamics model cause the origami structure to deviate from the ideal kinematic path, as shown in the folding angle plots The ideal path is traced more closely at first, with only slight deviation caused by nodal damping Oscillations arise when folding angle limits are reached and the panels bounce back The structure then settles to a steady state Fig. 4d plots angles against angle θ' of a chosen crease, which is annotated in Fig. 4b, alongside ideal kinematic solutions of the Miura-ori pattern, further highlighting how the folding angles deviate slightly from the ideal solution due to transient dynamics, but converge towards correct final values at the steady state.

Appendix A details how using a quasi-static scheme instead of the dynamic scheme enables perfect reproduction of ideal rigid folding The dynamics model is chosen instead however, for its robustness, applicability for both rigid-foldable and non-rigid patterns, and its compatibility with dynamic relaxation In fact, robust modelling of dynamic phenomena using the implicit Euler scheme is a key enabler for the dimensional and configuration synthesis capabilities of the proposed direct inverse design method.

2.4. Contact Modelling

In many origami patterns, contact happens not between adjacent panels that share a common crease, but between non-adjacent panels These scenarios cannot be captured by simple folding angle limits and therefore require additional modelling Work on contact modelling in bar-hinge models exists [75], but does not cover all possible collision scenarios, specifically the edge-edge case and the point-edge case illustrated in Fig. 5.

By exploiting the fact that bar-hinge models already require triangulation of panels for their structure modelling, panel collision can be considered solely as triangle-triangle collision Depending on the geometric configuration of panels, three distinct collision scenarios exist By simple geometric considerations, these scenarios can be identified, and restoring forces can be modelled for each case.

Fig. 5 first illustrates the process by which collision scenarios are identified Two triangles labelled 1 and 2 are considered here, representing any panel pair in a bar-hinge model First, triangle-triangle intersection detection is computed between the two triangles This is completed by computing the line-triangle intersection for each edge of triangle 1 and the face of triangle 2, and vice versa Denoting the number of intersected edges of triangles 1 and 2 as $n_{col,1}$ and $n_{col,2}$ respectively, it can be shown that only two possibilities exist, either $\Sigma n_{col} = 0$, which means the triangle pairs are collision-free, or $\Sigma n_{col} = 2$, which indicates collision.

In the case of collision, two more possibilities exist, either $n_{col,1} = n_{col,2} = 1$, which corresponds to a case which is referred to here as *edge-edge* collision, or $n_{col,1} \neq n_{col,2}$, which leads to further possibilities Either $n_{col,1} = 2$ and $n_{col,2} = 0$, which means a corner of triangle 1 has cut into the face of triangle 2, or $n_{col,1} = 0$ and $n_{col,2} = 2$, which is where triangle 2 has cut into triangle 1 For conciseness, only the former is illustrated here.

Considering the motion trajectory of panels, there are again two possibilities Triangle 1 could have come from an out-of-plane direction and cut point-first into the face of triangle 2, or it could have come from an in-plane direction and cut into a side of triangle 2 Both cases result in the same instantaneous scenario, and swift identification is needed for computational efficiency, ideally not using information from the previous time step To achieve this, three distances are considered The minimum distance between the intersecting point on triangle 1 and the plane of triangle 2 is computed as d_1, while the minimum distances between the intersecting edges on triangle 1 and the edge of triangle 2 are

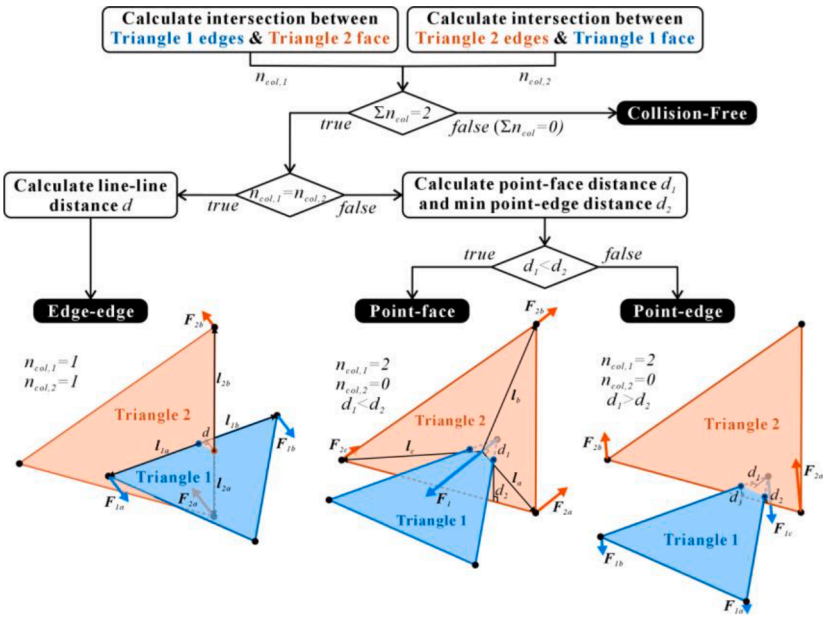

Fig. 5. Identification and modelling of the three distinct collision scenarios which can arise between a pair of triangular panels.

calculated as d_2 and d_3, with $d_2 < d_3$ If d_1 is smaller than d_2, it can be inferred that triangle 1 came from an out-of-plane direction, and this case is referred to as *point-face* collision Alternatively, if d_2 is smaller than d_1, triangle 1 most likely came from an in-plane direction, leading to a case denoted as *point-edge* collision.

For contact modelling, restoring forces must be considered for each case This allows the dynamic bar-hinge model to respond to collisions, exerting forces that push panels back, similar to the real world Appendices C–E detail benchmark cases and technical details regarding each contact case Considering first the edge-edge collision case, the restoring force is considered proportional to the minimum distance between the intersecting edges A simple moment equilibrium condition is considered in order to distribute this restoring force to the two end nodes of each edge This results in four nodal forces, denoted as $\boldsymbol{F}_{1a}$, $\boldsymbol{F}_{1b}$, $\boldsymbol{F}_{2a}$ and $\boldsymbol{F}_{2b}$, respectively, which satisfy

$$\begin{cases} \boldsymbol{F}_{1a} + \boldsymbol{F}_{1b} = -(\boldsymbol{F}_{2a} + \boldsymbol{F}_{2b}) \propto d, \\ \boldsymbol{l}_{1a} \times \boldsymbol{F}_{1a} + \boldsymbol{l}_{1b} \times \boldsymbol{F}_{1b} = 0, \\ \boldsymbol{l}_{2a} \times \boldsymbol{F}_{2a} + \boldsymbol{l}_{2b} \times \boldsymbol{F}_{2b} = 0, \end{cases} \tag{16}$$

where $\boldsymbol{l}_{1a}$, $\boldsymbol{l}_{1b}$, $\boldsymbol{l}_{2a}$, and $\boldsymbol{l}_{2b}$ are the moment arms of the restoring forces from the points of minimum distance along the collided edges Summing these nodal forces into the bar-hinge model provides the necessary restoring force for the edge-edge case Appendix C details benchmark cases as well as example cases which demonstrate the validity of this formulation.

For the point-face case, the restoring force is considered proportional to the minimum distance between the intersecting point of triangle 1 and the face of triangle 2 The force on triangle 1 is simply applied to the intersecting point as a nodal force $\boldsymbol{F}_1$, and the forces on triangle 2 are again computed using moment equilibrium All three nodes of triangle 2 need to exert force to counteract $\boldsymbol{F}_1$ and achieve moment balance Considering these nodal forces as $\boldsymbol{F}_{2a}$, $\boldsymbol{F}_{2b}$ and $\boldsymbol{F}_{2c}$, the constraining equations are

$$\begin{cases} \boldsymbol{F}_{2a} + \boldsymbol{F}_{2b} + \boldsymbol{F}_{2c} = -\boldsymbol{F}_1 \propto \mathrm{d}_1, \\ \boldsymbol{l}_a \times \boldsymbol{F}_{2a} + \boldsymbol{l}_b \times \boldsymbol{F}_{2b} + \boldsymbol{l}_c \times \boldsymbol{F}_{2c} = 0, \end{cases} \tag{17}$$

where $\boldsymbol{l}_i$ refers to the moment arm of $\boldsymbol{F}_{2i}$ from the intersecting point of vector $\boldsymbol{F}_1$ and triangle 2 Note that friction is neglected, so restoring forces can be assumed to be perpendicular to triangle 2 The moment balance equation is linear, and can be easily solved to yield the magnitudes of $\boldsymbol{F}_1$, $\boldsymbol{F}_{2a}$, $\boldsymbol{F}_{2b}$ and $\boldsymbol{F}_{2c}$, returning the required nodal forces which can be summed into the bar-hinge model Relevant benchmark cases and examples can be found in Appendix D.

For the point-edge case, it can be observed that d_2 and d_3 each correspond to an edge-edge collision, so it can be easily modelled using two superposed edge-edge contact models which return 5 restoring nodal forces Benchmark cases and examples for the point-edge case can be found in Appendix E.

In all cases, the contact modelling methods used are able to correctly capture the precise contacts between the panels Panels realistically bounce back upon collision, and settle into steady states which respect panel contacts The implicit Euler scheme is able to robustly proceed with the nonlinearities introduced by collision, providing the necessary modelling foundation for dynamic relaxation.

3. Inverse design using dynamic relaxation

With a robust bar-hinge model and complete contact modelling at hand, the foundation for dynamic relaxation computation is now in place, and a direct inverse design method can be developed Inverse design of origami structures entails adjusting their crease patterns and folding to fulfil design objectives, which are most often prescribed geometries for the folded or partially-folded states The design method must accommodate such objectives, respect isometry and collision constraints, and be as computationally efficient as possible.

To this end, this paper proposes a new coupled dynamic relaxation method Design objectives are imposed as equivalent external forces, and isometry constraints are enforced by directly coupling the equilibrium lengths of bars in each state Compared to existing methods, this method requires minimal manual analysis for each design case More importantly, the method employs a single forward computation process Compared to optimizer-based methods which require a large number of iterations, or dynamic relaxation with explicit enforcement of equality constraints which requires convergence at each step, the current method offers higher computational efficiency This section details the formulation of the dynamic relaxation scheme and then demonstrates its capabilities in dimensional synthesis, configuration synthesis, and the design of multi-configuration morphing origami structures.

3.1. Dynamic relaxation scheme formulation

Direct inverse design using dynamic relaxation generates optimal crease patterns by allowing the structure to evolve towards a state of minimum strain energy under imposed loads and boundary conditions Unlike conventional structures, origami structures fold into multiple states with the same bar length but different hinge angles Fig. 6a details the computation process for the dynamic relaxation direct inverse design method developed here The overall process is very similar to that of the aforementioned dynamic bar-hinge forward model, with but two key differences.

First, design objectives and constraints are translated into external forces imposed on the bar-hinge structure For example, surface-fitting objectives can be translated into surface-normal forces that guide nodes towards the target surface, and collision constraints are also injected here as contact forces By adding equivalent forces, the structure's minimum strain energy state will satisfy the design objectives, and dynamic relaxation will allow the structure to naturally evolve towards that design This formulation is akin to Lagrange multipliers in gradient descent schemes, and avoids the use of explicit equality constraints which require expensive convergence computation.

Second, equilibrium lengths of bar elements are reassigned at each time step as the observed instantaneous mean bar length across multiple specified states These specified states are used to describe desired configurations For example, the folded and unfolded states of an origami structure can be computed in parallel By setting the equilibrium bar length of a bar in all states as the mean length of that bar across states, bar lengths all converge towards the mean value and naturally evolve to satisfy isometry constraints, again avoiding explicit equality constraints Essentially, bar strain from the mean bar length provides an equivalent gradient that guides the evolution of the origami structure's geometry.

Fig. 6 details the step-by-step workflow of dynamic relaxation with bar length coupling Initialization commences separately for states S_i, where nodal coordinates $\left[\boldsymbol{s}_{x0}^{S_i}, \boldsymbol{s}_{y0}^{S_i}, \boldsymbol{s}_{z0}^{S_i}\right]$ are prescribed, velocities $\boldsymbol{v}^{S_i}$ are set as zero, while nodal accelerations $\boldsymbol{a}^{S_i}$, folding angles $\boldsymbol{\theta}^{S_i}$ and bar lengths $\boldsymbol{L}_0$ can be derived from nodal coordinates Actuation angles $\boldsymbol{\theta}_0|_{t_i}^{S_i}$ and external forces $\boldsymbol{F}_{ext}|_{t_i}^{S_i}$ are set as time-dependent parameters, so that they can be ramped gradually to guide the structure towards desired shapes, without inducing excessive accelerations and transient behaviours Actuation angles can be used alongside the aforementioned equivalent external forces to describe design objectives For example, certain creases can be required to be flat or fully folded, which can be conveniently described by $\theta_0 = 0^\circ$ and $\theta_0 = 180^\circ$.

Next, updating coupled bar lengths is the key step that enforces isometry constraints For each bar, its bar length is simply computed as

$$L_0 = \frac{1}{n}\sum_{i}^{n} L|_{t_i}^{S_i}, \tag{18}$$

where $L|_{t_i}^{S_i}$ denotes the bar length observed in each state S_i at the current time step This is applied as an artificial step in the numerical scheme, and is not fully described within the dynamics model, i.e., the implicit Euler scheme simply observes an instant change in L_0 at each step, without modelling length as a separate state with dynamic behaviour Owing to the unconditional numerical stability of the implicit Euler scheme, such an artificial step has no impact on the robustness or precision of the overall dynamic relaxation scheme, and results can be recovered efficiently.

After updating bar length, the updating of derivatives and the implicit Euler scheme using a trust-region solver are identical to those of the dynamic bar-hinge forward model Note that each state is solved independently, without any further exchange of information between the states The only carrier of information across states is the mean bar length of Eq. (18) After sufficient time, the structure is guaranteed to stabilise at a steady-state solution, driven not only by direct nodal damping, but also by the artificial damping introduced by the implicit Euler scheme.

Fig. 6b and 6c illustrate the surface-normal forces which are used to enforce surface fitting objectives for parametric surfaces The expressions for planes, cylindrical surfaces, spheres, and saddle surfaces are expressed in Cartesian form, while revolute surfaces are expressed in polar coordinate form The normal vectors of these surfaces are also formulated accordingly After applying a stiffness of choice, surface-normal forces can be derived as an attractive force towards the target surface The closed-form descriptions of these forces allow subsequent stiffness and Jacobian matrices to be constructed directly, as in the bar-hinge model, thereby maintaining computational efficiency With regard

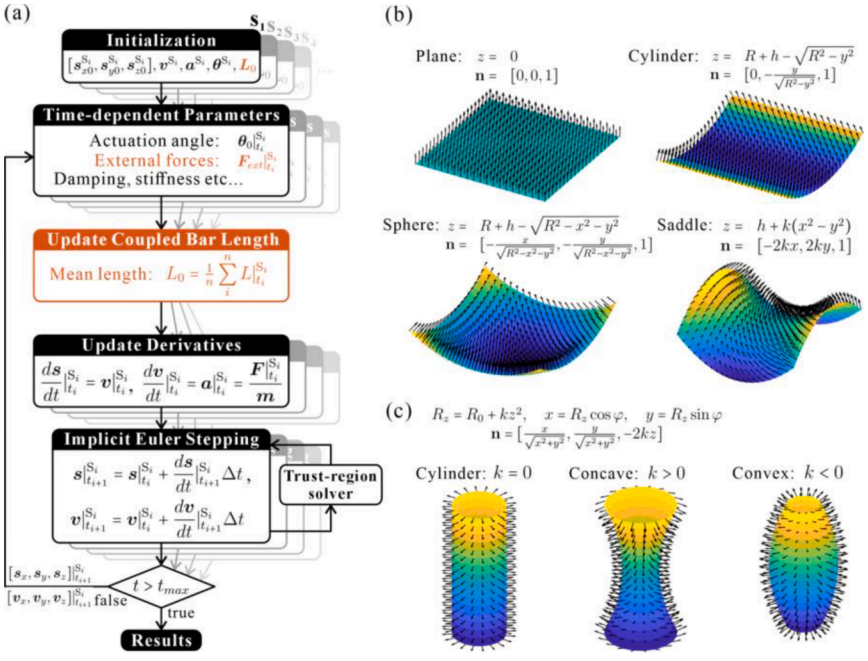

Fig. 6. Direct inverse design using dynamic relaxation (a) Computation scheme where bar length coupling is applied through mean bar length updating (b) Surface-normal forces describing parametric Cartesian surface fitting objectives (c) Surface-normal forces describing revolute surface fitting objectives.

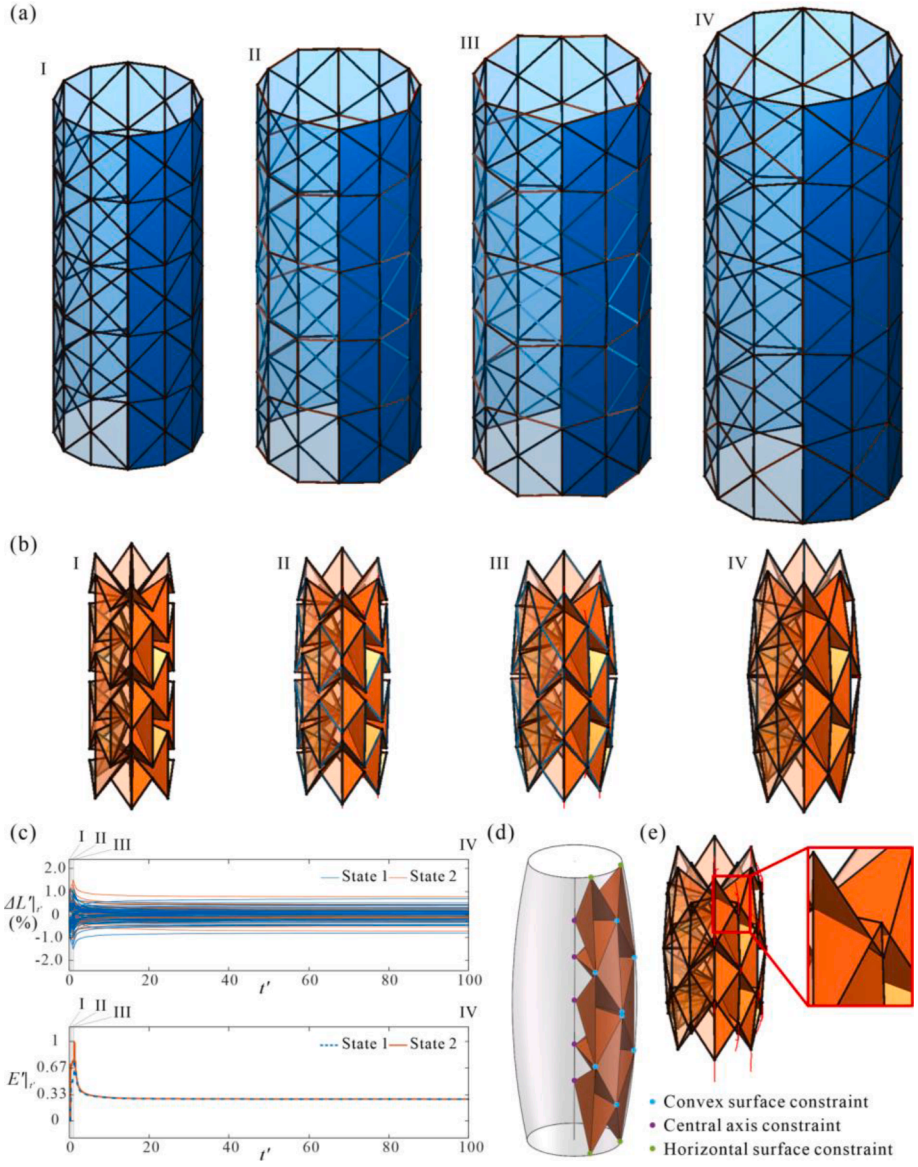

Fig. 7. Dimensional synthesis of a Waterbomb pattern with a cylindrical unfolded state and a convex folded state A corresponding video can be found in the supporting information (a) Evolution of the unfolded state (b) Evolution of the folded state (c) Relative length discrepancy and total strain energy during dynamic relaxation (d) Illustration of imposed constraints (e) Result from dynamic relaxation without contact modelling, where physical interference occurs.

to direct inverse design, developability and flat-foldability constraints can also be enforced by constraining a state using plane normal forces Such forces also provide a level of flexibility to the design When objectives require strict adherence, stronger surface-normal forces can be applied When the design problem is complex or objectives are conflicting, applying slightly weaker surface-normal forces allows the structure to not only converge more quickly but also self-adjust to a shape that balances competing objectives In all, the overall dynamic relaxation process solves an inverse design problem without using any external optimisers in a single forward computation.

3.2. *Dimensional synthesis of origami structures*

The dynamic relaxation scheme is intended to perform dimensional synthesis of origami structures The multiple states of an origami structure evolve in parallel towards a desired shape Simultaneous adjustment of all nodal coordinates is performed, which is equivalent to adjusting the dimensions of all panels and creases For typical origami patterns, this involves dozens if not hundreds of independent variables and multiple design objectives, covering at least the folded and unfolded states This section demonstrates how dimensional synthesis can be efficiently performed to produce optimal results.

Fig. 7 displays an example design problem using a Waterbomb origami pattern, conceptualised for origami-based coronary stents The design objectives include: (1) The unfolded state is to be cylindrical, i.e zero Gaussian curvature, so that it may be fabricated from a planar sheet (2) The folded state is to have a convex exterior profile, while the inner nodes of the Waterbomb pattern are to be along the central axis (3) The vertical creases in the pattern are to be fully folded, i.e have 180° folding angle.

To maximise computation efficiency, a single section of the 6-section Waterbomb pattern is modelled here This restricts the design problem to 25 unique vertices, whose Cartesian coordinates are equivalent to 75 design variables To enforce periodic boundary conditions, attractive forces are applied between node pairs, with the addition of a rotation transformation An additional half-section is included, so that all folding angles can be modelled The key surface constraints for the folded state are illustrated in Fig. 7d The outer nodes are guided towards a convex surface by equivalent external forces, while the inner nodes are guided towards the central axis These nodes are free to move along the surface or axis At

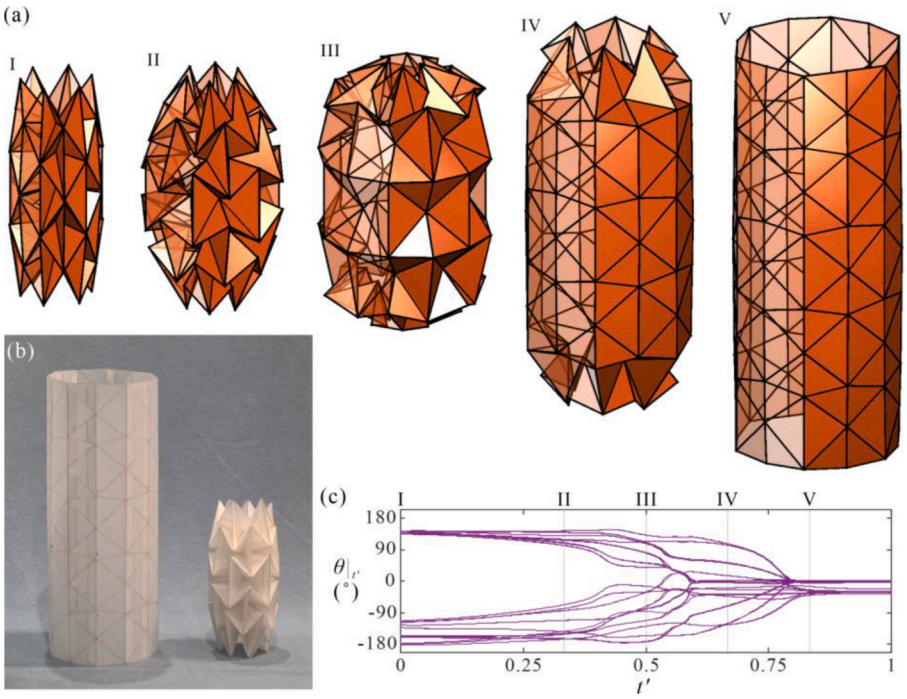

Fig. 8. Unfolding of the generated Waterbomb pattern from the convex folded state to the cylindrical unfolded state (a) Unfolding process of the overall structure (b) Paper prototype displaying the folded and unfolded states (c) Corresponding folding angles computed for the unfolding process.

the top and bottom edges, an additional horizontal surface constraint is applied For the unfolded state, nodes are constrained to have equal radius The mean radius of all nodes is calculated at each time step, and nodes are guided towards a cylinder of that radius This applies the cylindrical shape constraint without constraining the cylinder's radius.

Fig. 7a and 7b display the evolution of the unfolded and folded states, with corresponding length discrepancy and strain energy displayed in Fig. 7c External forces and folding angle actuations are ramped between $t' = 0$ and $t' = 1$, where t' is normalised time Afterwards, the structure is allowed to relax until $t' = 100$ Normalised length discrepancies $\Delta L'$ are the difference between a bar's length in the unfolded and folded states, expressed as a percentage of total length Normalised strain energy E' is the sum of bar and hinge strain energies in the entire structure It can be observed that both rise as the structure is gradually loaded, then decay exponentially towards a steady state Note that neither values converge towards zero, meaning a trade-off is completed between the conflicting objectives imposed here The dynamic relaxation procedure is able to naturally find the best trade-off solution through evolution.

Finally, Fig. 7e displays a result when the aforementioned contact modelling within the bar-hinge model is omitted Physical interference between panels is observed As the Waterbomb pattern evolves, the minimum-energy path leads it to a geometric configuration in which non-adjacent panels collide This is not captured by folding angle limits, so with the absence of contact modelling, the panels pass through one another into an invalid minimum-energy state Conversely, when contact modelling is included, it can be seen in state IV of Fig. 7b that the panels contact one another at their edge, without further intersection.

Fig. 8 details the unfolding of the resulting Waterbomb structure Here, all hinges are actuated towards the unfolded state, simulating the deployment of an elastic-energy-driven stent The structure begins from its convex folded state and unfolds into the expected cylinder shape, following a process similar to that analysed for non-rigid Waterbomb patterns [76] As Fig. 8b shows, paper prototypes were also fabricated to validate the geometry of the generated origami structure The prototype consists of 170 gramme per square metre tear-resistant card stock, with creases etched using a laser cutter.

3.3. Configuration synthesis of origami structures

Apart from dimensional synthesis, the dynamic relaxation scheme is capable of generating folding configurations that are not designed a priori This is owing to the implicit Euler scheme's ability to accommodate highly non-linear phenomena, allowing the structure to deform across local minimum states, into states of global minimum energy Such changes in folding configurations are coupled with changes in origami structure dimension, and therefore are difficult to design using other methods This section demonstrates how configuration synthesis can also be completed by the dynamic relaxation method.

Fig. 9 displays a second example design problem using the Waterbomb origami pattern The design objectives include: (1) The unfolded state is to be concave, so that the resulting stent may fit the profile of certain arteries (2) The folded state is to have a cylindrical exterior profile, while the inner nodes of the Waterbomb pattern are to be along the central axis (3) The vertical creases in the pattern are to be fully folded The topology and in fact the initial shape of the Waterbomb origami pattern is unchanged from that in Fig. 7, with 25 unique vertices corresponding to 75 equivalent design variables However, the geometric conditions of the design objectives imposed here dictate that a valid solution can no longer be obtained through adjustments to dimensions only As seen in Fig. 9b, a twist in the origami structure emerges from the dynamic relaxation process, accommodating panels in the folded state.

Figs. 9a and 9b display the evolution of the unfolded and folded states, with corresponding length discrepancy and strain energy displayed in Fig. 9c The external forces and folding angles are again ramped until $t' = 1$ and held Afterwards, a swifter relaxation is observed, terminating at $t' = 20$ It is during this relaxation process, across states II, III, and IV, that the twisted configuration of the folded structure is formed A significant jump in both bar length discrepancy $\Delta L'$ and strain energy E' can be observed near state III, where the structure turns towards the twisted configuration Twisting of the Waterbomb pattern has been discussed in previous research [77], and is independently generated here by dynamic relaxation as a method to accommodate panels, without any deliberate injection of design knowledge In fact, it was not known beforehand that twists are necessary for the concave structure here.

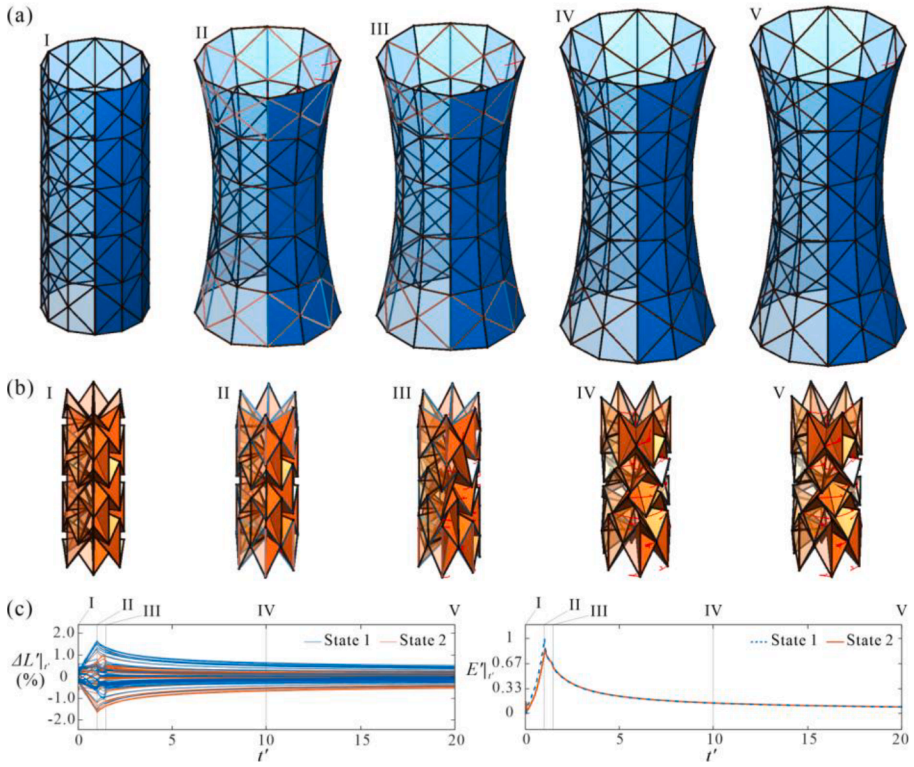

Fig. 9. Configuration synthesis of a Waterbomb pattern with a cylindrical folded state and concave unfolded state A corresponding video can be found in the supporting information (a) Evolution of the unfolded state (b) Evolution of the folded state (c) Relative length discrepancy and strain energy during dynamic relaxation.

Fig. 10 details the simulated concave Waterbomb structure Again, all hinges are actuated towards the unfolded state The structure begins from its cylindrical folded state and unfolds into the expected concave shape along a non-rigid folding path It can be observed how the twist unravels as the entire structure unfolds Again, paper prototypes show that the generated geometry is valid.

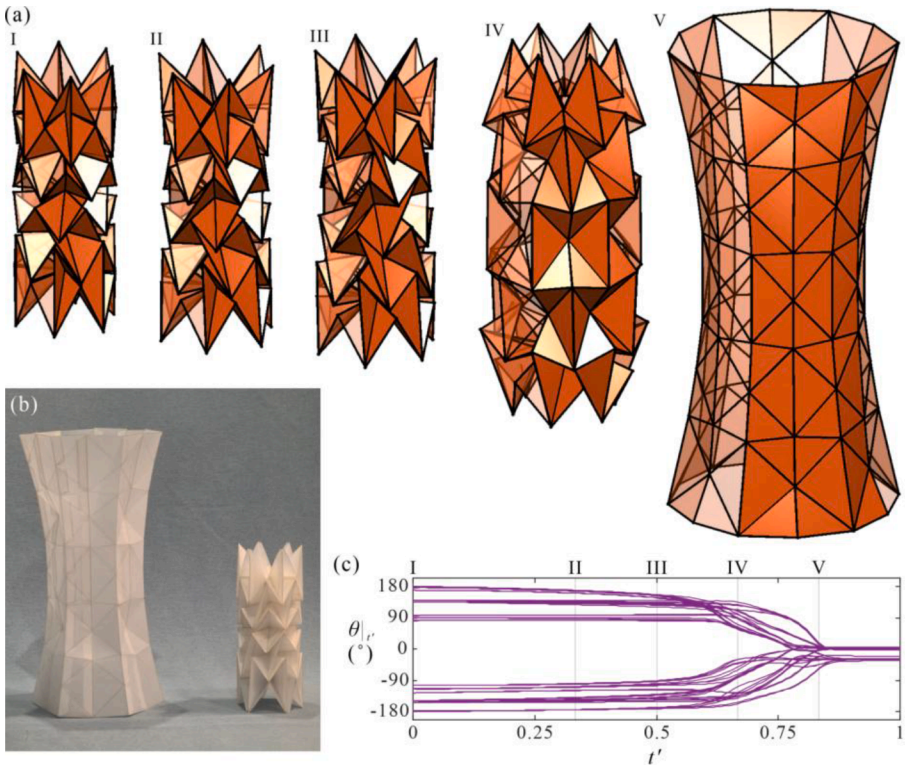

Fig. 10. Unfolding of the generated Waterbomb pattern from the cylindrical folded state to the concave unfolded state (a) Unfolding process of the overall structure (b) Paper prototype displaying the folded and unfolded states (c) Corresponding folding angles computed for the unfolding process.

3.4. Multi-configuration morphing origami structure

The coupled dynamic relaxation method developed here can readily accommodate more than just two states, raising the possibility of designing multi-configuration origami structures To demonstrate this, a multi-configuration morphing Resch origami structure is designed.

The triangular Resch pattern used here contains 61 vertices, corresponding to 183 equivalent design variables As shown in Fig. 11a, four target surfaces are imposed in four separate states A flat plane in the first state enforces developability, while the latter three states enforce a spherical surface, a saddle surface, and a cylindrical surface respectively In addition to surface fitting constraints, folding angle constraints were also applied to certain creases To maintain a fixed outer boundary for the folded Resch pattern, which provides better structural integrity, creases along the boundary are pinched at a prescribed 180° folding angle Initial geometries are simply the original triangular Resch pattern with identical tessellated panels Surface-normal forces and hinge forces are exerted on relevant vertices of the patterns in each state, pushing them into the final shape shown in Fig. 11b The resulting crease pattern is displayed in Fig. 11c, overlayed onto the initial pattern The differences before and after dynamic relaxation can be observed Pinched creases corresponding to folding angle constraints are also marked.

The length difference and energy evolution during dynamic relaxation is plotted in Fig. 11d The surface-normal forces are ramped with normalised time t', in between t'=0 and t'=1 This is done by gradually morphing the target surface from flat to the prescribed shape, providing guidance to the structure normalised length differences $\Delta L'$ and normalised energy E' both experience a corresponding initial rise and exponential decay Fig. 11e shows the fabricated physical prototype The pinched creases are maintained at 180° folding angle using adhesives Once folded, the prototype can freely morph between the spherical, saddle, and cylindrical states.

Certain features can be highlighted within the synthesised design Morphing is entirely accommodated by the triangular stars of the Resch pattern While the boundary creases have been pinched, these stars are allowed to open and close, changing the overall form of the entire pattern In the saddle state, all stars are fully closed, meaning at least two of the three radial creases reach 180° folding angle, eliminating any degree of freedom As the stars open, the overall structure is free to morph into the other two states.

To experimentally validate the resulting design, geometric information of the paper prototype is extracted, so that quantitative comparison may be conducted The model is placed on a 3D printed mount, and a 3D Scanner (Artec Space Spider, scanning accuracy of 0.05 mm) is

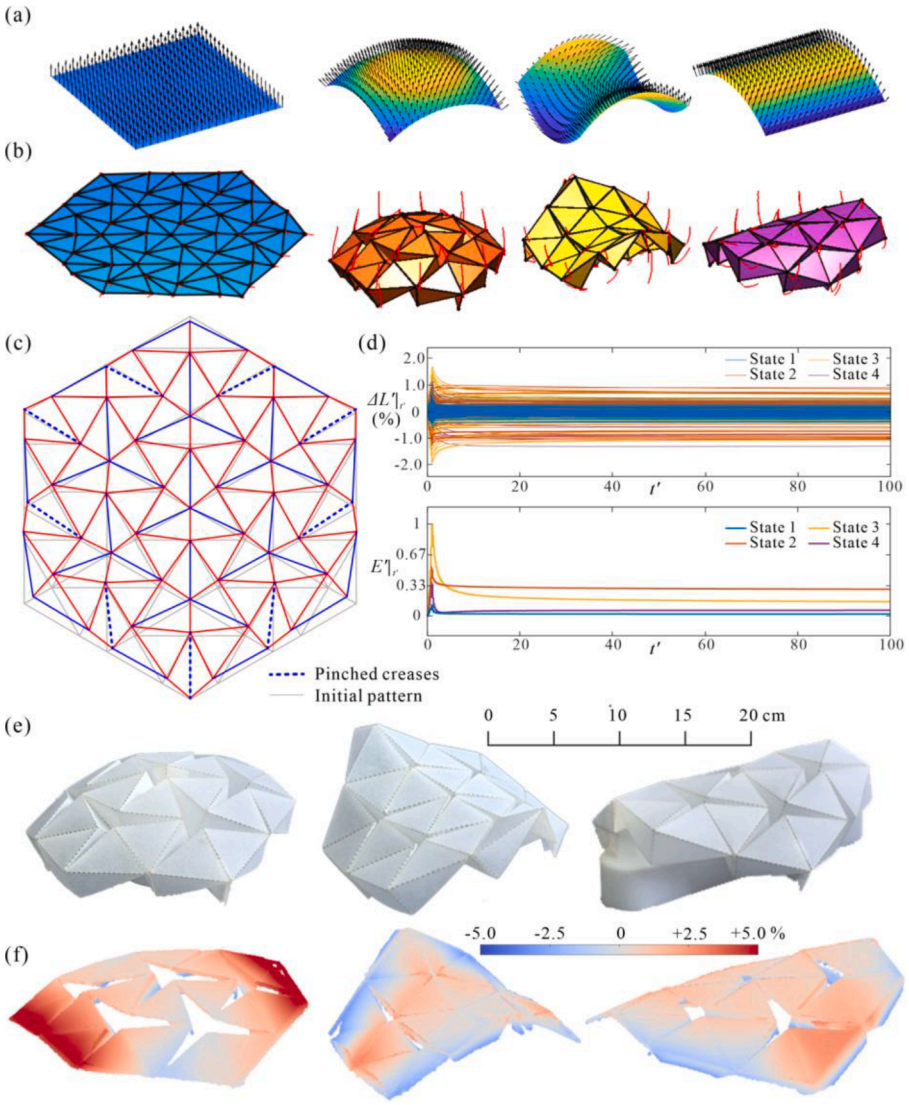

Fig. 11. Synthesis of a multi-configuration morphing Resch pattern A corresponding video can be found in the supporting information (a) Target surfaces (b) Ideal design after dynamic relaxation (c) Resulting pattern geometry overlayed on the initial pattern geometry (d) Relative length discrepancy and strain energy during dynamic relaxation (e) Paper prototype of the resulting design (f) Deviation of the prototype from the ideal design.

used to produce a digital reconstruction of the geometry Fig. 11f displays the z-direction deviation of the manufactured prototype from the ideal design, i.e., the output in Fig. 11b Deviations in the model arise from manufacturing imperfections and are expressed as a percentage of the total model size The spherical state experiences the most deviation, at around 5%, which appears at the edges This is due to residual strain in the paper prototype causing unwanted deformation, which affects surface fitting In the saddle and cylindrical states, far lower deviation is observed, as the Resch pattern's stars are closed, making the structure better constrained In addition to the Resch pattern, origami structures such as the well-studied Miura-ori pattern can also be synthesised for multiple configurations An additional design case can be found in Appendix F In all, the dynamic relaxation method is capable of producing designs which accommodate numerous design objectives and the isometry constraints imposed by multiple folding configurations.

4. Conclusions

This paper presents a direct inverse design methodology for origami structures that addresses the challenges associated with complex design objectives and constraints By integrating dynamic relaxation with isometry constraints enforced through bar length coupling, and translating design objectives and constraints into equivalent external forces, the proposed approach eliminates the need for iterative optimization or explicit enforcement of equality constraints, enabling efficient form-finding in a single forward computation.

Under the proposed inverse design scheme, complex surface fitting objectives are incorporated as external surface-normal forces, while a comprehensive contact force modelling scheme effectively handles all possible panel collision scenarios to enforce interference constraints The implicit Euler scheme employed for solving the dynamic relaxation problem ensures robust capture of highly nonlinear behaviours with minimal computational cost Through force-based representation of objectives and constraints, the method achieves simultaneous dimensional and configurational synthesis of origami structures.

The successful synthesis of multiple origami structures, including multi-configuration examples, demonstrates the versatility and practical applicability of the proposed framework for simultaneous dimensional and configuration synthesis of origami structures In addition, the bar-hinge model employed by this method extends its applicability beyond origami structures to encompass truss, membrane, and tensegrity structures, all of which admit a bar-hinge representation This work aims to provide a new tool for the direct inverse design of origami structures and offers a generalizable foundation for extending these principles to the design of other structures.

CRediT authorship contribution statement

Tianshu Wang: Writing – original draft, Software, Methodology, Investigation, Formal analysis, Conceptualization. **Zhitao Su:** Validation, Investigation. **Wenli Liu:** Validation, Investigation. **Jiayao Ma:** Writing – review & editing, Supervision, Methodology, Funding acquisition, Conceptualization. **Yan Chen:** Writing – review & editing, Supervision, Methodology, Funding acquisition, Conceptualization.

Declaration of competing interest

The authors declare that they have no known competing financial interests or personal relationships that could have appeared to influence the work reported in this paper.

Acknowledgments

This work is supported by the National Natural Science Foundation of China (Projects 52320105005, 52422502, 52192631).

Supplementary material

Supplementary material associated with this article can be found, in the online version, at doi:10.1016/j.ijmecsci.2026.111864.

Appendix A Quasi-static simulation

Quasi-static simulations are useful for accurate modelling of rigid-foldable origami By removing any dynamic effects, it is possible to accurately trace the kinematic trajectory taken by rigid-foldable origami mechanisms To retain the bar-hinge formulation and unify with other models, a force equilibrium model is used This is illustrated in Fig. A1a.

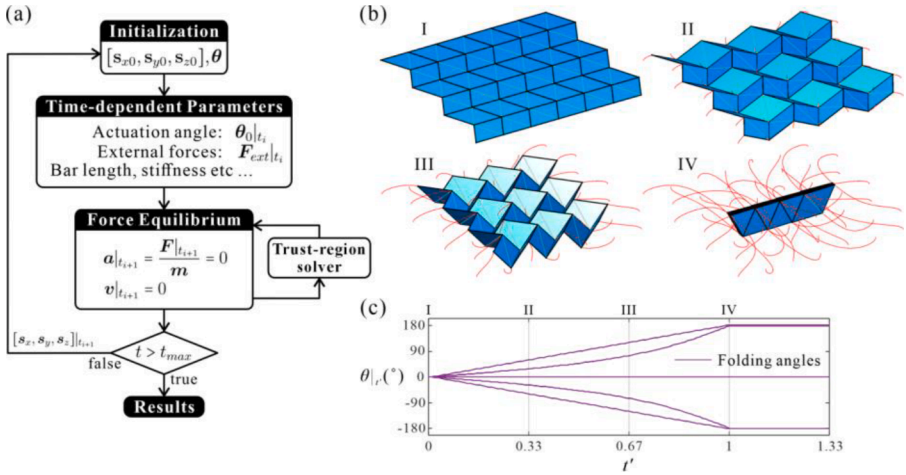

Fig. A1. Quasi-static modelling and example results of a Miura-ori pattern (a) Computation scheme based on nodal force equilibrium (b) Folding simulation of the Miura-ori structure (c) Folding angles which correspond exactly with the theoretical kinematic solution.

Initialization defines the starting position of the simulation Initial coordinates $[s_{x0},s_{y0},s_{z0}]$ are adopted, and initial folding angles $\boldsymbol{\theta}$ can be calculated Note that these values are vector values that encapsulate all vertices and creases in the pattern Stepping forward, time-dependent parameters including actuation angles $\boldsymbol{a}|_{t_i}$ and external forces $\boldsymbol{F}_{ext}|_{t_i}$ can be expressed according to the specific simulation task Other values, including bar length and stiffness, can also be altered in the bar-hinge model, allowing versatile simulation capabilities Force equilibrium involves solving instantaneous coordinate values $[s_x,s_y,s_z]$ which must satisfy

$$\boldsymbol{a}|_{t_i} = \frac{\boldsymbol{F}|_{t_i}}{\boldsymbol{m}} = 0 \tag{A1}$$

Because a quasi-static assumption is used, velocities are assigned to zero, negating any inertial or damping effects The valid values of $[s_x,s_y,s_z]$ are numerically obtained using a trust region solver (MATLAB *fsolve*) The target scenarios considered here are mainly rigid-foldable origami, which have smooth kinematics, so such a force-equilibrium scheme is adopted to harmonise with dynamic bar-hinge models For highly non-linear scenarios, including snap-through behaviours, this scheme will not converge, and dynamic simulations are recommended instead.

Figure A1b shows illustrative results of a Miura-ori pattern The actuation angles of mountain and valley creases, denoted as black edges, are linearly ramped from 0° to ± 180°, and a large stiffness is applied to creases within quadrilateral panels, denoted as grey edges, to preserve panel flatness Folding angles $\boldsymbol{\theta}$ are plotted against normalised time t', and it can be observed that folding angles closely follow the ideal kinematic path expected from Miura-ori patterns, and are free of any oscillatory behaviour or deviations.

Appendix B folding angle limit modelling

Folding angle limits are enforced by a piece-wise linear torsion spring constitutive model As introduced in the main text, restoring torque is applied by a superposed torsion spring with significant stiffness once the folding angle exceeds limits Fig. B1 presents an illustrative case where folding angle limits influence simulation results The spiral quadrilateral origami pattern [78] simulated here contains geometrically similar panels that are scaled sequentially, leading to the root (smaller) panels reaching 180° folding angle before the subsequent panels When angle limits are not applied, the root panels exceed 180°, which is incorrect This is shown in Fig. B1a, where the trajectory exceeding 180° is annotated in red When angle limits are applied, the folding process correctly stops at 180°.

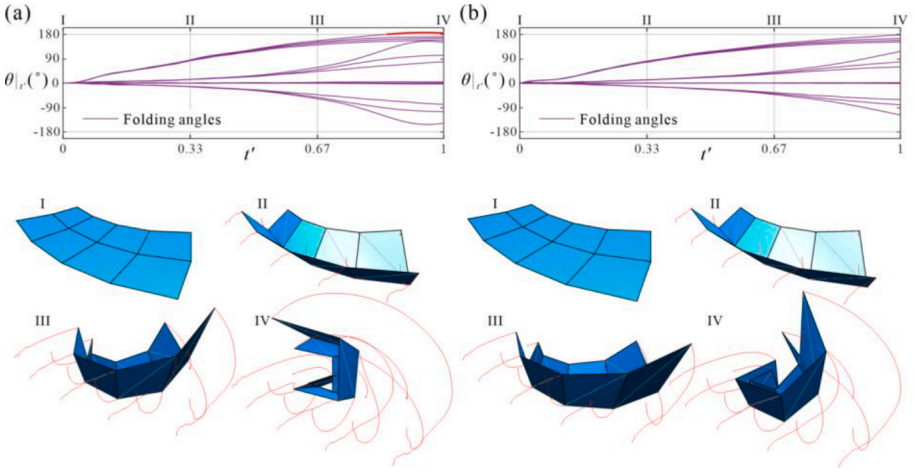

Fig. B1. Folding angle limit modelling of a spiral origami pattern (a) Simulation without contact (b) Simulation with contact.

Appendix C edge-edge contact modelling

Edge-edge contact is illustrated in Fig. C1a As the main text introduced, restoring forces are proportional to the minimum distance between the two intersecting edges and are distributed according to moment equilibrium A benchmark case is presented below, where Fig. C1b plots folding angles and nodal acceleration magnitudes, while Fig. C1c illustrates the folding process The centre quadrilateral panel of this benchmark case is fixed, and one neighbouring triangular panel is sprung upwards until it collides with the other triangular panel Motion can first be observed via θ_1, then initial contact occurs in state III, where θ_2 begins to shift, and significant accelerations can be observed Pushing behaviour between the two panels can be correctly observed as well.

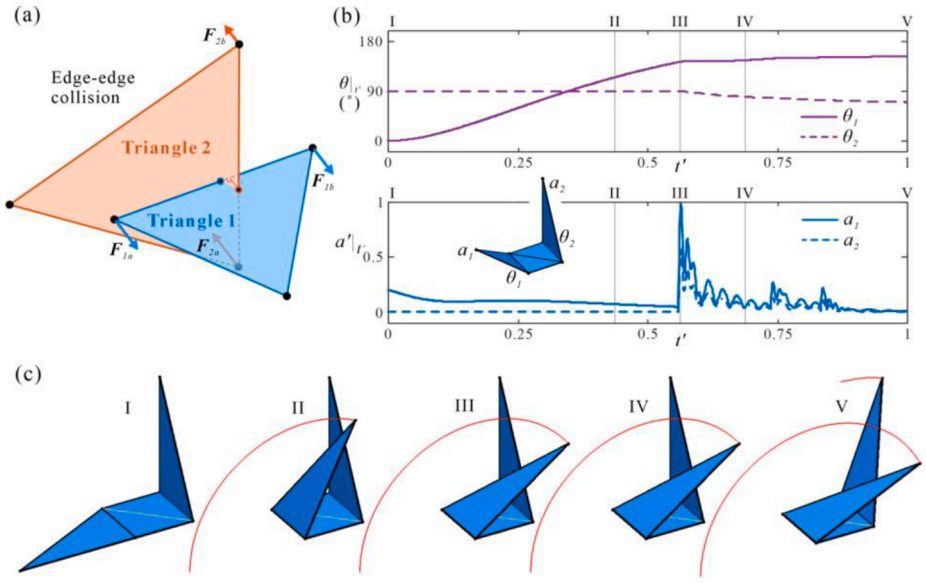

Fig. C1. Edge-edge contact model for a pair of triangular panels (a) Illustration of key parameters (b) Benchmark case folding angle and acceleration results (c) Benchmark case folding process.

Edge-edge contact can also be found in more complex origami structures Here, another spiral origami pattern with geometrically similar quadrilateral panels [78] is modelled When folding, opposing panels contact one another at their edges The effect of edge-edge contact modelling is illustrated below, where Fig. C2a shows how panels intersect when contact is not modelled, and Fig. C2b shows how contact modelling leads to folding being correctly stopped, and how spikes in acceleration can be correctly captured by the implicit Euler numerical scheme.

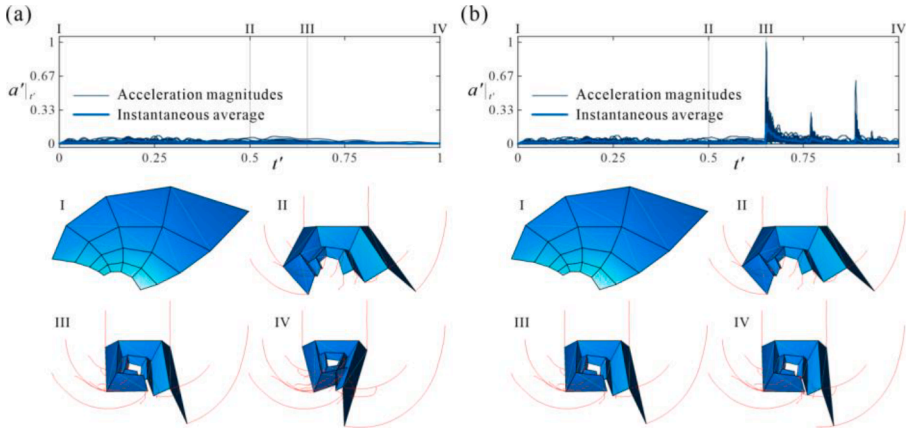

Fig. C2. Edge-edge contact modelling of a spiral origami pattern (a) Simulation without contact (b) Simulation with contact.

Appendix D point-face contact modelling

Point-face contact is illustrated in Fig. D1a As the main text introduced, restoring forces are proportional to the minimum distance between the intersecting point and the corresponding face, and again distributed according to moment equilibrium A benchmark case is shown below, where Fig. D1b plots folding angles and nodal accelerations, while Fig. D1c illustrates the folding process A similar configuration consisting of a centre quadrilateral panel and neighbouring triangular panels is used, and panel geometry is slightly altered to produce point-face contact Initial motion can also be observed via θ_1, and initial contact occurs in state III It can be observed how the point contacts the opposing face, pushing it away while also leading to compression of panel edges neighbouring the point.

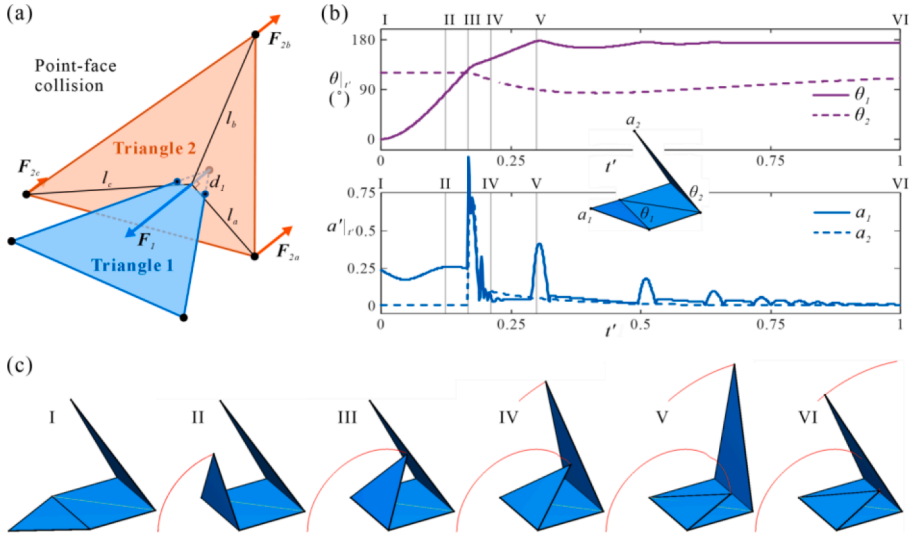

Fig. D1. Point-face contact model for a pair of triangular panels (a) Illustration of key parameters (b) Benchmark case folding angle and acceleration results (c) Benchmark case folding process.

Point-face contact is again benchmarked using a spiral origami pattern, which is in fact identical to that in Fig. C2 An alternative mountain-valley crease assignment [79] leads to a different folding configuration where opposing panels collide with point-face contact The effect of point-face contact modelling is illustrated below, where Fig. D2a shows how panels intersect when contact is not modelled, and Fig. D2b shows how contact modelling leads to folding being correctly stopped, and how the overall origami pattern folds into a triangular configuration.

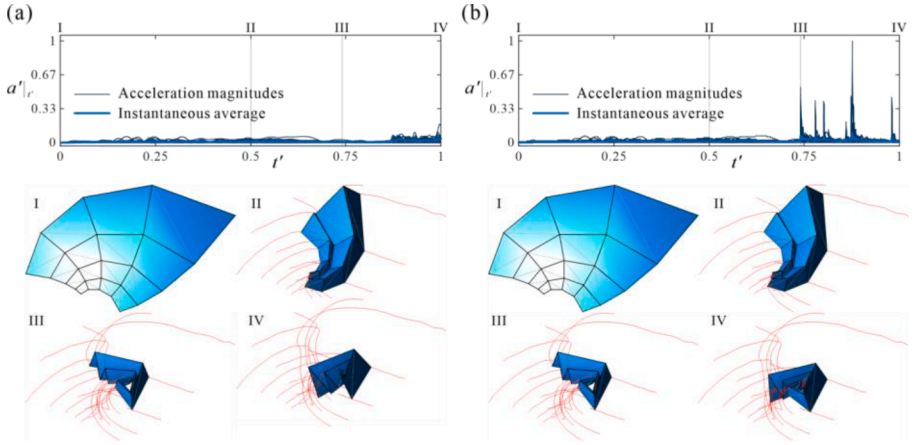

Fig. D2. Point-face contact modelling of a spiral origami pattern (a) Simulation without contact (b) Simulation with contact.

Appendix E point-edge contact modelling

Point-edge contact is illustrated in Fig. E1a As the main text introduced, this case is essentially two superposed edge-edge contacts Correspondingly, contact stiffness is halved for each edge-edge contact, so the overall point-edge contact behaviour is retained A benchmark case is presented below, where Fig. E1b plots folding angles and nodal accelerations, while Fig. E1c illustrates the folding process A second quadrilateral panel is used here, replacing one triangular panel so that point-edge contact occurs Motion can again be observed via θ_1, and initial contact occurs in state III The triangular panel is parallel with the edge it collides with, so even if smaller time-steps were to be used, the triangular panel will inevitably overshoot the edge and entirely cut into the quadrilateral panel, necessitating the point-edge contact case here to be differentiated from a point-face case Here it can be observed how the triangular panel is correctly stopped by the edge, and how pushing between panels occurs.

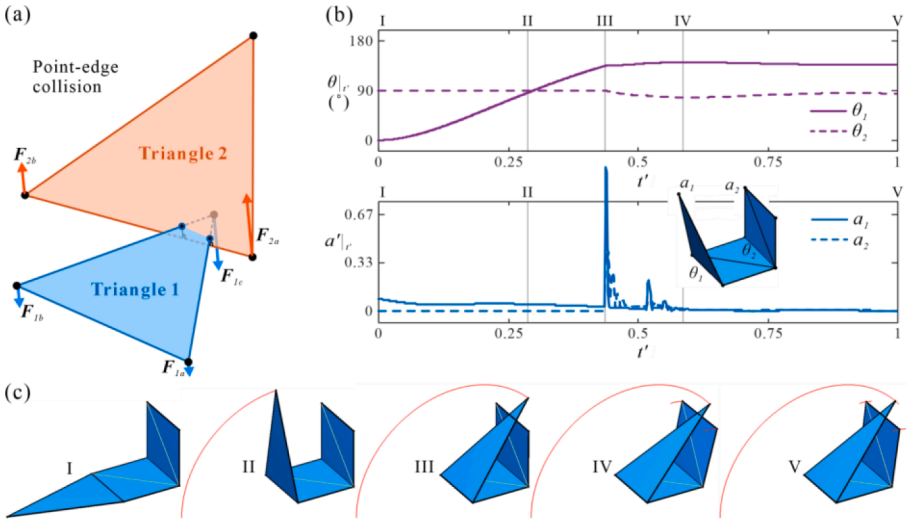

Fig. E1. Point-edge contact model for a pair of triangular panels (a) Illustration of key parameters (b) Benchmark case folding angle and acceleration results (c) Benchmark case folding process.

Point-edge contact mainly arises as edge cases which sporadically arise at certain time-steps In the arc-Miura pattern [80], however, it is a driving phenomenon Panels on opposing sides of the pattern collide with one another, and due to the geometry of the arc-Miura pattern, tend to contact in the point-edge mode The effect of point-edge contact modelling is illustrated below, where Fig. E2a shows how panels intersect when contact is not modelled, and Fig. E2b shows how contact modelling leads to folding being correctly stopped, and how the panels rest in a forked configuration.

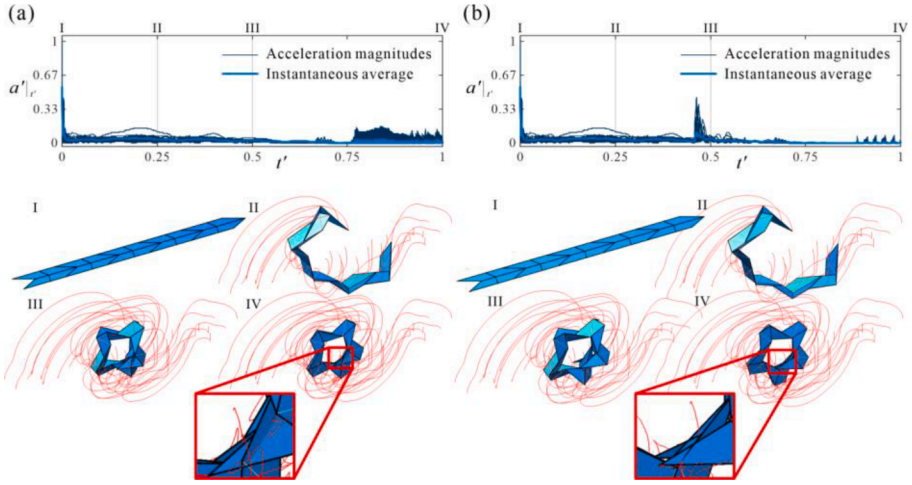

Fig. E2. Point-edge contact modelling of an arc-Miura origami pattern (a) Simulation without contact (b) Simulation with contact.

Appendix F design of a multi-configuration Miura-ori structure

The Miura-ori pattern is one of the most seminal origami patterns to date, simultaneously possessing developability, flat-foldablity, and rigid-foldablity Previous works have extensively studied its surface-fitting capabilities, showing that the Miura-ori pattern can retain developability and flat-foldability whilst fitting target surfaces in its partially folded state While existing works use a dedicated system of simultaneous equations, solving the same problem using dynamic relaxation offers advantages in convenience and efficiency The Miura-ori pattern used here contains 49 vertices, corresponding to 147 design variables The design results are shown in Fig. F1 Three simultaneous configurations are used The first states is the flat unfolded state, where out-of-plane normal forces constrain vertices to only move in plane, enforcing developability The second state is the flat-folded state, where similar out-of-plane forces enforce flat-foldability The third state is a partially folded state, where the top vertices of the Miura-ori pattern are constrained to a spherical surface, using normal forces illustrated in Fig. 6b The quadrilateral panels are kept flat by adding a large stiffness to the diagonal bar-hinge element, enforcing rigid-foldability Figure F1d shows the generated pattern, and relevant paper models are included in Fig. F1f By generating the Miura-ori pattern as a multi-configuration origami structure, common properties including developability and flat-foldability can be conveniently enforced under the dynamic relaxation framework.

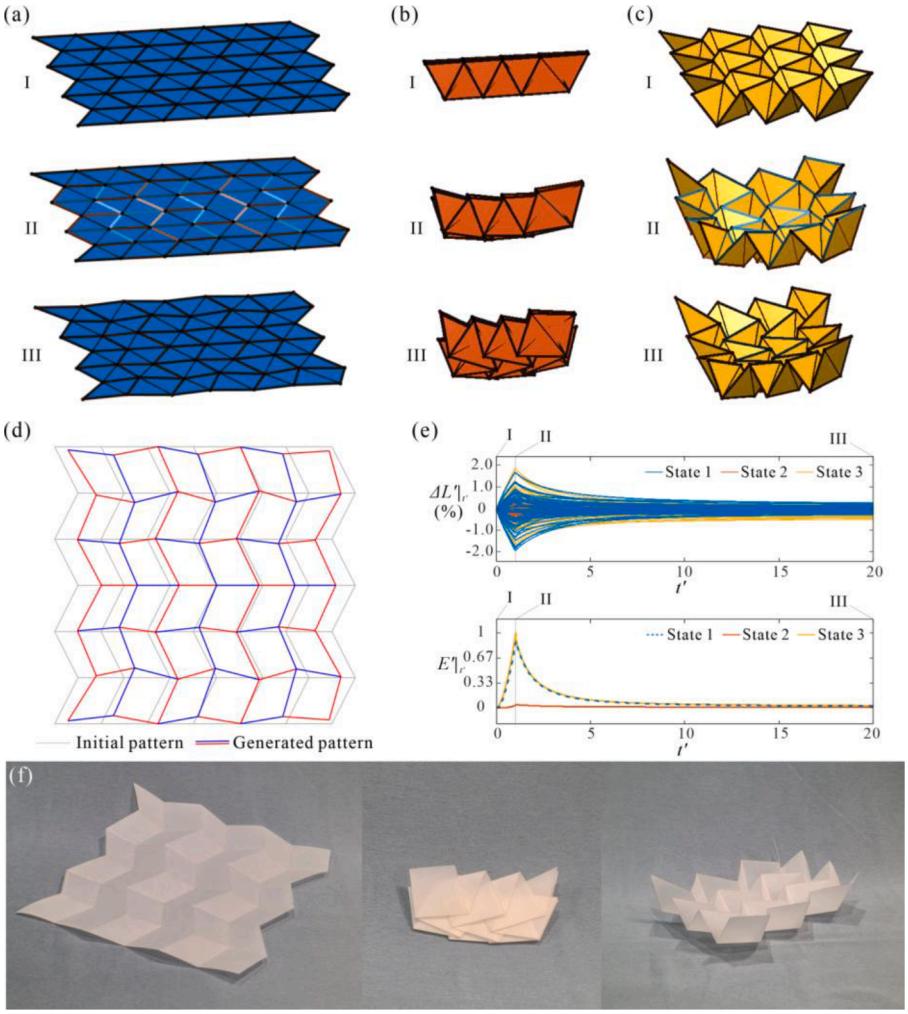

Fig. F1. Synthesis of a multi-configuration Miura-ori pattern A corresponding video can be found in the supporting information (a) Evolution of the flat unfolded state (b) Evolution of the flat-folded state (c) Evolution of the partially folded state which approximates a spherical surface (d) Resulting pattern geometry overlayed on the initial pattern geometry (e) Relative length discrepancy and strain energy during dynamic relaxation (f) Paper prototype of the resulting design.

Data availability

Data will be made available on request.

References

[1] Arya M, Webb D, McGown J, Lisman PD, Shaklan S, Bradford SC, Steeves J, Hilgemann E, Trease B, Thomson M, Warwick S, Freebury G, Gull J. Starshade mechanical design for the habitable exoplanet imaging mission concept (habex). SPIE Optical Engineering+ Applications, 10400. SPIE; 2017. p. 1–14.

[2] Kuriki K, Ninomiya K, Takei M, Matsuoka S. Lessons learned from the space flyer unit (SFU) mission. Acta Astronaut 2002;51(11):797–806. https://doi.org/10.1016/S0094-5765(02)00026-7.

[3] Ikeya K, Sakamoto H, Nakanishi H, Furuya H, Tomura T, Ide R, Iijima R, Iwasaki Y, Ohno K, Omoto K, Furuya T, Hayashi T, Kato M, Koide S, Kurosaki M, Nakatsuka Y, Okuyama S, Kashiyama R, Nakamura J, Nio W, Tsunemitsu T, Yamazaki Y, Taga K, Hohmann B, Amamoto T, Chubachi T, Tamura S, Okada H, Watanabe A, Kawabata N, Hori T, Ito H, Kuratomi T, Shimoda Y, Hidaka N, Watanabe K, Torisaka A, Yamazaki M. Significance of 3u cubesat origamisat-1 for space demonstration of multifunctional deployable membrane. Acta Astronaut 2020;173:363–77. https://doi.org/10.1016/j.actaastro.2020.04.016.

[4] Dufour L, Datashvili LS, Guinot F, Legay H, Goussetis G. Origami deployable reflector antenna for cubesats. AIAA scitech 2021 forum, aiaa scitech forum. American Institute of Aeronautics and Astronautics; 2021. https://doi.org/10.2514/6.2021-1703.

[5] Reis PM, Jiménez FL, Marthelot J. Transforming architectures inspired by origami. Proc Natl Acad Sci USA 2015;112(40):12234–5. https://doi.org/10.1073/pnas.1516974112.

[6] Meloni M, Zhang Q, Cai J, Lee DS-H. Origami-based adaptive facade for reducing reflected solar radiation in outdoor urban environments. Sustain Cities Soc 2023;97:104740. https://doi.org/10.1016/j.scs.2023.104740.

[7] Chen Y, Feng H, Ma J, Peng R, You Z. Symmetric waterbomb origami. Proc R Soc A: Math Phys Eng Sci 2016;472(2190):20150846. https://doi.org/10.1098/rspa.2015.0846.

[8] Zhao W, Li N, Liu L, Leng J, Liu Y. Origami derived self-assembly stents fabricated via 4d printing. Compos Struct 2022;293:115669. https://doi.org/10.1016/j.compstruct.2022.115669.

[9] Wang C, Guo H, Liu R, Deng Z, Chen Y, You Z. Reconfigurable origami-inspired multistable metamorphous structures. Sci Adv 2024;10(22):eadk8662. https://doi.org/10.1126/sciadv.adk8662.

[10] He J, Wen G, Liu J, Xue L, Xie YM. A modular continuous robot constructed by miura-derived origami tubes. Int J Mech Sci 2024;261:108690. https://doi.org/10.1016/j.ijmecsci.2023.108690.

[11] Felton S, Tolley M, Demaine E, Rus D, Wood R. A method for building self-folding machines. Science (1979) 2014;345(6197):644–6. https://doi.org/10.1126/science.1252610.

[12] Chai S, Wang T, Xi K, Ma J, Chen Y. Design of a one-dof rigid-foldable wrapping origami pattern. Int J Mech Sci 2026;309:111009. https://doi.org/10.1016/j.ijmecsci.2025.111009.

[13] Zhang Y, Zhang X, Li M, Chen Y. The rigid and flat-foldable kirigami cubes. Int J Mech Sci 2024;282:109605. https://doi.org/10.1016/j.ijmecsci.2024.109605.

[14] Wang S, Wu J, Yan P, Huang H, Li B, Liu R. Design of deployable circular structures based on miura origami pattern. Mech Mach Theory 2023;186:105350. https://doi.org/10.1016/j.mechmachtheory.2023.105350.

[15] Li X, Huang H, Yan P, Wang W. Design and analysis of rigid-elastic coupling origami flashers with bistable characteristics. Int J Mech Sci 2024;282:109602. https://doi.org/10.1016/j.ijmecsci.2024.109602.

[16] Wang X, Qu H, Guo S. Tristable property and the high stiffness analysis of kresling pattern origami. Int J Mech Sci 2023;256:108515. https://doi.org/10.1016/j.ijmecsci.2023.108515.
[17] Zhang J, Chen J, Zhang X, Liu S, Wang C. A review of kresling origami: smart design, mechanics, and applications. Eng Struct 2025;345:121499. https://doi.org/10.1016/j.engstruct.2025.121499.
[18] Chai S, Hu Z, Chen Y, You Z, Ma J. Programmable multistability of curved-crease origami structures with travelling folds. J Mech Phys Solids 2024;193:105877. https://doi.org/10.1016/j.jmps.2024.105877.
[19] Hussain KF, Cantwell W, Khan KA. Curved-crease origami hybrid structures with tailorable buckling and energy absorption. Int J Mech Sci 2024;284:109724. https://doi.org/10.1016/j.ijmecsci.2024.109724.
[20] Sun Y, Song K, Ju J, Zhou X. Curved-creased origami mechanical metamaterials with programmable stabilities and stiffnesses. Int J Mech Sci 2024;262:108729. https://doi.org/10.1016/j.ijmecsci.2023.108729.
[21] Yu Y, Hong T-CK, Economou A, Paulino GH. Rethinking origami: a generative specification of origami patterns with shape grammars. Comput.-Aided Des 2021;137:103029. https://doi.org/10.1016/j.cad.2021.103029.
[22] Walker A, Stankovic T. Algorithmic design of origami mechanisms and tessellations. Commun Mater 2022;3(1):4. https://doi.org/10.1038/s43246-022-00227-5.
[23] Meloni M, Zhang Q, Cai J. Exploratory design method for origami pattern generation in engineering applications. Engineering 2025. https://doi.org/10.1016/j.eng.2025.10.025.
[24] Demaine ED, Tachi T. Origamizer: a practical algorithm for folding any polyhedron. In: Aronov B, Katz M J, editors. 33rd International Symposium on Computational Geometry (SoCG 2017), Vol 77 of Leibniz International Proceedings in Informatics (LIPIcs). Schloss Dagstuhl–Leibniz-Zentrum für Informatik; 2017. https://doi.org/10.4230/LIPIcs.SoCG.2017.34. 34:1–34:16.
[25] Zirbel SA, Lang RJ, Thomson MW, Sigel DA, Walkemeyer PE, Trease BP, Magleby SP, Howell LL. Accommodating thickness in origami-based deployable arrays1. J Mech Des 2013;135(11). https://doi.org/10.1115/1.4025372.
[26] Tachi T. Freeform variations of origami. J Geom Graph 2010;14. 01.
[27] Tachi T. Designing freeform origami tessellations by generalizing Resch's patterns. J mech des 2013;135(11):111006.
[28] Suto K, Noma Y, Tanimichi K, Narumi K, Tachi T. Crane: an integrated computational design platform for functional, foldable, and fabricable origami products. ACM Trans Comput.-Hum Interact Sep 2023;30(4). https://doi.org/10.1145/3576856.
[29] Dudte LH, Vouga E, Tachi T, Mahadevan L. Programming curvature using origami tessellations. Nat Mater 2016;15(5):583–8. https://doi.org/10.1038/nmat4540.
[30] Hu Y, Zhou Y, Liang H. Constructing rigid-foldable generalized miura-ori tessellations for curved surfaces. J Mech Robot 2020;13(1). https://doi.org/10.1115/1.4048630.
[31] Tachi T. Generalization of rigid foldable quadrilateral mesh origami. J Int Assoc Shell Spat Struct 2009;50. 12.
[32] Dang X, Feng F, Plucinsky P, James RD, Duan H, Wang J. Inverse design of deployable origami structures that approximate a general surface. Int J Solids Struct 2022;234-235:111224. https://doi.org/10.1016/j.ijsolstr.2021.111224.
[33] Wang T, Santer M. Rigid-foldable parabolic deployable reflector concept based on the origami flasher pattern. J Spacecr Rockets 2023. https://doi.org/10.2514/1.A35497.
[34] T Wang, M Santer, Rigid-foldable doubly curved deployable reflectors based on the Miura–Ori pattern, J Spacecr Rockets 0 (0) 1–17 doi:10.2514/1.A36107.
[35] McAdams DA, Li W. A novel method to design and optimize flat-foldable origami structures through a genetic algorithm. J Comput Inf Sci Eng 2014;14(3):031008. https://doi.org/10.1115/1.4026509.
[36] Grey SW, Scarpa F, Schenk M. Embedded actuation for shape-adaptive origami. J Mech Des 2021;143(8):081703. https://doi.org/10.1115/1.4049880.
[37] Wang T, Gu Y, Chen Y. Shape-reconfigurable deployable paraboloid reflector based on a 7r-8r truss network. Chin J Mech Eng 2025;38(1):124. https://doi.org/10.1186/s10033-025-01302-x.
[38] Chen Y, Yan J, Feng J, Sareh P. Particle swarm optimization-based metaheuristic design generation of non-trivial flat-foldable origami tessellations with degree-4 vertices. J Mech Des 2020;143(1):011703. https://doi.org/10.1115/1.4047437.
[39] Chen Y, Lu C, Yan J, Feng J, Sareh P. Intelligent computational design of scalene-faceted flat-foldable tessellations. J Comput Des Eng 2022;9(5):1765–74. https://doi.org/10.1093/jcde/qwac082.
[40] Day A. An introduction to dynamic relaxation(dynamic relaxation method for structural analysis, using computer to calculate internal forces following development from initially unloaded state). engineer 1965;219:218–21.
[41] Barnes MR. Form finding and analysis of tension space structures by dynamic relaxation. Ph.D thesis. City University London; 1977. October.
[42] Barnes M. Form finding and analysis of tension structures by dynamic relaxation. Int J Space Struct 1999;14(2):89–104. https://doi.org/10.1260/0266351991494722.
[43] Alic V, Persson K. Form finding with dynamic relaxation and iso-geometric membrane elements. Comput Methods Appl Mech Eng 2016;300:734–47. https://doi.org/10.1016/j.cma.2015.12.009.
[44] Ji-hong Y, Shu-lu Z. The modified dynamic relaxation method for form-finding of membrane structures. Eng Mech 2008;25(12):194–201.
[45] He J, Wang Y, Li X, Jiang H, Ye Z. A modified dynamic relaxation form-finding method for general tensegrity structures with inextensible tensile members. Comput Struct 2024;291:107204. https://doi.org/10.1016/j.compstruc.2023.107204.
[46] Nagano Y, Nagai T. Form-finding and structural modeling of membrane-tensegrity composite structures with proposal for highly feasible model. In: Proceedings of the IASS Symposium 2024 Redefining the Art of Structural Design. International Association for Shell and Spatial Structures (IASS); 2024. p. 1–10. paper 289.
[47] Wang X, Cai J, Yang R, Feng J. Form-finding of deployable mesh reflectors using dynamic relaxation method. Acta Astronaut 2018;151:380–8. https://doi.org/10.1016/j.actaastro.2018.06.017.
[48] Khatibinia M, Hosseinaei S, Sarafrazi SR. Efficiency of dynamic relaxation methods in form-finding of tensile membrane structures. SN Appl Sci 2019;1(11):1502. https://doi.org/10.1007/s42452-019-1529-6.
[49] Haraszti A, Arya M. Curved-crease origami wrapping of doubly curved shells using coupled dynamic relaxation. AIAA Scitech 2025 Forum. 2025. p. 1–17. https://doi.org/10.2514/6.2025-0618.
[50] Miki M, Adriaenssens S, Igarashi T, Kawaguchi K. The geodesic dynamic relaxation method for problems of equilibrium with equality constraint conditions. Int J Numer Methods Eng 2014;99(9):682–710. https://doi.org/10.1002/nme.4713.
[51] Denavit J, Hartenberg RS. A kinematic notation for lower-pair mechanisms based on matrices. J Appl Mech 2021;22(2):215–21. https://doi.org/10.1115/1.4011045.
[52] Zhang X, Chen Y. The diamond thick-panel origami and the corresponding mobile assemblies of plane-symmetric bricard linkages. Mech Mach Theory 2018;130:585–604. https://doi.org/10.1016/j.mechmachtheory.2018.09.005.
[53] Zhao C, Li M, Zhou X, Liu T, Xing J, Chen Y, Zhang X. Deployable structure based on double-layer miura-ori pattern. Mech Res Commun 2023;131:104152. https://doi.org/10.1016/j.mechrescom.2023.104152.
[54] Huang Z, Liu J, Zeng D. A general methodology for mobility analysis of mechanisms based on constraint screw theory. Sci China E: Technol Sci 2009;52(5):1337–47. https://doi.org/10.1007/s11431-008-0219-1.
[55] Gu Y, Zhang X, Wei G, Chen Y. Hamiltonian-path based constraint reduction for deployable polyhedral mechanisms. Mech Mach Theory 2024;193:105563. https://doi.org/10.1016/j.mechmachtheory.2023.105563.
[56] Tachi T. Simulation of rigid origami. Origami 2009;4(08):175–87.
[57] Wu W, You Z. Modelling rigid origami with quaternions and dual quaternions. Proc R Soc A: Math Phys Eng Sci 2010;466(2119):2155–74. https://doi.org/10.1098/rspa.2009.0625.
[58] Yang F, Chen Y, Kang R, Ma J. Truss transformation method to obtain the non-overconstrained forms of 3d overconstrained linkages. Mech Mach Theory 2016;102:149–66. https://doi.org/10.1016/j.mechmachtheory.2016.04.005.
[59] Kresling B. Natural twist buckling in shells: from the hawkmoth's bellows to the deployable kresling-pattern and cylindrical miura-ori. In: 6th International Conference on Computation of Shell and Spatial Structures; 2008. p. 1–10.
[60] Liu K, Tachi T, Paulino GH. Invariant and smooth limit of discrete geometry folded from bistable origami leading to multistable metasurfaces. Nat Commun 2019;10(1):4238. https://doi.org/10.1038/s41467-019-11935-x.
[61] Parque V, Suzaki W, Miura S, Torisaka A, Miyashita T, Natori M. Packaging of thick membranes using a multi-spiral folding approach: flat and curved surfaces. Adv Space Res 2021;67(9):2589–612. https://doi.org/10.1016/j.asr.2020.09.040.
[62] Mitani J. The folded shape restoration and the rendering method of origami from the crease pattern. In: Proceeding International Conference on Geometry and Graphics; 2008. p. 1–7.
[63] Chen H, Chai S, Ma J. Energy absorption of the kirigami-inspired pyramid foldcore sandwich structures under low-velocity impact. Int J Mech Sci 2024;284:109774. https://doi.org/10.1016/j.ijmecsci.2024.109774.
[64] Li M, Zhou Z, Hao B, Yu C, Chen Y, Ma J. Design and deformation analysis of an inflatable metallic cylinder based on the kresling origami pattern. Thin-Walled Struct 2023;188:110859. https://doi.org/10.1016/j.tws.2023.110859.
[65] Schenk M, Guest SD, et al. Origami folding: a structural engineering approach. Origami 2011;5:291–304.
[66] Filipov E, Liu K, Tachi T, Schenk M, Paulino G. Bar and hinge models for scalable analysis of origami. Int J Solids Struct 2017;124:26–45. https://doi.org/10.1016/j.ijsolstr.2017.05.028.
[67] Liu K, Paulino GH. Merlin : a matlab implementation to capture highly nonlinear behavior of non-rigid origami. In: Proceedings of the IASS Annual Symposium 2016; 2016. p. 1–10.
[68] Liu K, Paulino GH. Nonlinear mechanics of non-rigid origami: an efficient computational approach. Proc R Soc A: Math Phys Eng Sci 2017;473(2206):20170348. https://doi.org/10.1098/rspa.2017.0348.
[69] Ghassaei A, Demaine ED, Gershenfeld NA. Fast, interactive origami simulation using GPU computation. In: 7OSME - International Meeting on Origami in Science, Mathematics and Education; 2018. p. 1–16.
[70] Yu Y, Chen Y, Paulino G. Programming curvatures by unfolding of the triangular resch pattern. Int J Mech Sci. 2023;238:107861. https://doi.org/10.1016/j.ijmecsci.2022.107861.
[71] Woodruff SR, Filipov ET. A bar and hinge model formulation for structural analysis of curved-crease origami. Int J Solids Struct 2020;204-205:114–27. https://doi.org/10.1016/j.ijsolstr.2020.08.010.
[72] Tu GW, Filipov ET. Origami of multi-layered spaced sheets. J Mech Phys Solids 2024;190:105730. https://doi.org/10.1016/j.jmps.2024.105730.
[73] Lee T-U, Lu H, Ma J, Ha NS, Gattas JM, Xie YM. Self-locking and stiffening deployable tubular structures. Proc Natl Acad Sci USA 2024;121(40):e2409062121. https://doi.org/10.1073/pnas.2409062121.
[74] Tropp O, Tal A, Shimshoni I. A fast triangle to triangle intersection test for collision detection. Comput Animat Virtual Worlds 2006;17(5):527–35. https://doi.org/10.1002/cav.115.

[75] Zhu Y, Filipov ET. An efficient numerical approach for simulating contact in origami assemblages. Proc R Soc A: Math Phys Eng Sci 2019;475(2230):20190366. https://doi.org/10.1098/rspa.2019.0366.
[76] Ma J, Feng H, Chen Y, Hou D, You Z. Folding of tubular waterbomb. Research 2020;2020. https://doi.org/10.34133/2020/1735081.
[77] Feng H, Ma J, Chen Y, You Z. Twist of tubular mechanical metamaterials based on waterbomb origami. Sci Rep 2018;8(1):9522. https://doi.org/10.1038/s41598-018-27877-1.
[78] Chen Y, Lv W, Peng R, Wei G. Mobile assemblies of four-spherical-4r-integrated linkages and the associated four-crease-integrated rigid origami patterns. Mech Mach Theory 2019;142:103613. https://doi.org/10.1016/j.mechmachtheory.2019.103613.
[79] Liu W, Cao S, Chen Y. Mountain-valley crease reconfiguration of 4-crease origami vertices and tessellations. Int J Mech Sci 2024;273:109224. https://doi.org/10.1016/j.ijmecsci.2024.109224.
[80] X Zhang, Y Chen, Mobile assemblies of bennett linkages from four-crease origami patterns, Proc R Soc A: Math Phys Eng Sci 474 (2210) (2018) 20170621 doi:10.1098/rspa.2017.0621.